POROELASTIC AND POROPLASTIC MODELING OF HYDRAULIC FRACTURING

A Thesis

Presented to

the Faculty of the Department of Petroleum Engineering

University of Houston

In partial fulfillment of requirements for the degree of

Master of Science

in Petroleum Engineering

by

HanYi Wang

May 2014

POROELASTIC AND POROPLASTIC MODELING OF HYDRAULIC FRACTURING

_____

HanYi Wang

Approved:

_____

Chair of the Committee
Guan Qin, Associate Professor,
Department of Petroleum Engineering

Committee Members:

_____

XiuLi Wang, Adjunct Professor,
Department of Petroleum Engineering

_____

Thomas K. Holley, Professor and
Director of Department in Petroleum
Engineering

_____

Suresh K. Khator, Associate Dean,
Cullen College of Engineering

ACKNOWLEDGEMENTS

I would like to express my gratitude and appreciation to those who significantly contributed to this work. Only through their support and invaluable advice have I been able to complete the task.

I'm deeply thankful to Dr. Michael J. Economides, my mentor and thesis advisor, for his support, guidance and continued help throughout my research. The great experience to work with him is unforgettable. His hard work, acumen, intuitive instinct, entrepreneur spirit and fearless approaches to challenges will continue inspire me for the rest of my life.

I also would like to express my appreciation to Dr. Guan Qin, Dr. Thomas K. Holley, and Dr. XiuLi Wang for serving as my advisory committee.

Finally, I would like to thank all my family for their understanding and all my friends' support in my life.

POROELASTIC AND POROPLASTIC MODELING OF HYDRAULIC FRACTURING

An Abstract of a Thesis

Presented to

the Faculty of the Department of Petroleum Engineering

University of Houston

In partial fulfillment of requirements for the degree of
Master of Science

in Petroleum Engineering

by

HanYi Wang

May 2014

ABSTRACT

It is essential to predict the behavior of hydraulic fractures accurately based on the understanding of fundamental mechanisms, governing process. The prevailing approach for hydraulic fracture modeling relies on Linear Elastic Fracture Mechanics (LEFM) that gives reasonable predictions for hard rock hydraulic fracturing, but often fails to give accurate predictions of fracture geometry and propagation pressure in soft/unconsolidated formation. The reasons are that the fracture process zone ahead of the crack tip, elasto-plastic material behavior and strong coupling between flow and stress cannot be neglected in these formations.

In this study, we developed a fully coupled poroelastic and poroplastic hydraulic fracturing model with cohesive zone method. The impact of formation plastic properties on fracture process is investigated. The results indicate that formation plastic behavior can have a great impact on fracture net pressure and geometry, especially when the plastic deformation area is large.

TABLE OF CONTENTS

LIST OF FIGURES

LIST OF TABLES

1. INTRODUCTION

1.1 Hydraulic Fracturing

Hydraulic fracturing is an extensively used method of stimulating oil and gas reservoirs to enhance the production of hydrocarbons. In recent years as the technology of horizontal wells advanced and price of oil and gas increased, there is a boost in the application of hydraulic fracturing in the oil and gas industry, which makes it an interesting research topic. Modeling hydraulic fracture propagation is a challenging problem. The mathematical formulation of the problem is represented by a set of nonlinear integro-differential equations. Also, the problem has a moving boundary where the governing equations degenerate and become singular. The complexity of the problem often restricts researchers to consider only simple fracture geometries.

1.2 Hydraulic Fracture in Unconsolidated and Soft Formation

The prevailing approach for hydraulic fracture modeling relies on Linear Elastic Fracture Mechanics (LEFM). Generally, these methods, that use the stress intensity factor at the fracture tip, give reasonable predictions for hard rock hydraulic fracture processes, but fail to give accurate predictions of fracture geometry and propagation pressure in soft/unconsolidated formation. The reasons are that the fracture process zone ahead of the crack tip, elasto-plastic material behavior and strong coupling between flow and stress cannot be neglected in these formation.

The high permeability and porosity and low drained bulk modulus of unconsolidated formation result in a stronger coupling between the mechanical deformation and the pore pressure than is the case for consolidated rocks. Hence, the

process of fluid flow needs to be coupled with the mechanical response in order to better description of fracture propagation mechanisms in soft formations. In addition, the mechanical constitutive model must be elasto-plastic to model the post failure plastic yielding.

Although classic hydraulic fracturing simulators based on LEFM and analytical solutions are convenient to use and can give reasonable predictions for hard rock formation, there are still fundamental questions on adequacy of certain physical criteria (assumptions) used in the model and their effect on propagation regimes. One of them is inadequacy of LEFM approach to description of hydraulic fracture propagation in weakly consolidated/soft rock. Numerous laboratory studies have shown that deformation of very weak uncemented sands and shales can even occur through elastic-visco-plastic constitutive behavior, and the deformations of these types of rocks can't predicted by linear elasticity (Sone and Zoback 2011). Research works involving surveying on net pressures (difference between the fracturing fluid pressure and the far-field confining stress) indicated that the net pressures encountered in soft formation are on average 50–100% higher than the predicted ones based on LEFM, net pressure is even higher in poorly consolidated formations (Papanastasiou and Thiercelin 1993).

Horsrud (1982) studied the stress distribution around an injection well drilled through a poorly consolidated rock. He made his solution based on different elastic and plastic properties of the formation. The method he used is strength of material approach which cannot predict the opening of the fracture and its propagation. This approach just can give the fracture initiation pressure. The results show that plasticity causes a lower fracture

initiation pressure, by as much as 10% lower than the elastic solution, but it depends on Poisson's ratio and horizontal to vertical effective stress ratio.

Murdoch (1993c) uses linear elastic fracture mechanics (Irwin, 1957; Tada et al. 1985) to predict the pressure required for hydraulic fracture initiation. Murdoch observed that the pressure required to initiate the hydraulic fracture in soil is a function of the initial slot and the water content of the soil. It was the first application of linear elastic fracture mechanics for prediction of onset of hydraulic fracture in soil. The stress intensity factor for a penny shaped fracture is given as

$$K_I = \frac{2}{\pi} P_d \sqrt{\pi a} \ , \tag{1.1}$$

where K_I is stress intensity factor, P_d is the driving pressure and a is the half length of the fracture. Figure 1.4 shows that the fracture toughness calculated from the fracture initiation pressure seems to be independent of the length of the starter slot. Finally Murdoch concluded that the small-scale yielding criterion of linear elastic fracture mechanics appears to support the use of K_{Ic} to predict hydraulic fracturing in silty clay.

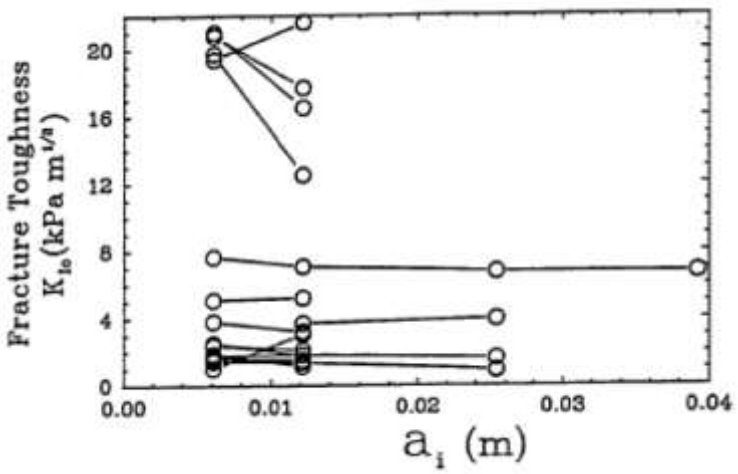

Figure 1.1 Fracture toughness as a function of the half length of the fracture opening (Murdoch, 1993a).

Murdoch (1993b) observed that when soil is saturated, K_{Ic} is essentially zero and well developed hydraulic fractures were not created in soils of negligible toughness. There is an upper limit of water content above which injection of glycerine will just form a bubble like feature rather than a fracture. Therefore, although K_{Ic} appears to be a useful indicator of the onset of propagation, it cannot predict conditions in which hydraulic fracture will not form.

Mori and Tamura (1987) and Jaworski et al. (1979) have done experiments on hydraulic fracturing in sand. Their aforementioned experiments do not have a starter slot like the experiments by Murdoch (1993) but the fluid is injected into an open cylindrical hole (open-hole completion). The pressure record from these experiments was found hard to duplicate presumably due to small preexisting cracks or pores intersected by the wellbore acting as the starter slot. Thus a_i (initial fracture half opening) was unknown and probably varied through different samples, so the effects of initial fracture size cannot be studied.

Papanastasiou and Thiercelin (1993) have studied the influence of inelastic rock behavior on hydraulic fracturing. They used the finite element method for solving the fracture propagation problem based on elastoplastic fracture mechanics (EPFM). The geometry of the problem is a simple KGD model. The numerical results suggest that the plastic effects in hydraulic fracturing result in a wider fracture with less fluid lag at the tip of the fracture. However, the fracture initiation pressure did not differentiate a lot for elastic and elastoplastic fracture cases.

The results show that plastic yielding near the tip of a propagating fracture provides an effective shielding, resulting in an increase in the rock effective fracture toughness by

more than an order of magnitude. Fig 1.5 shows that by increase toughness in elastic model we van match the net pressure in plastic formation.

Dam et al. (2000; 2001) have studied the impact of rock plasticity on hydraulic fracture propagation and closure based on theory and experiments. Figure 1.2 shows the plastic zone due to shear yield around the fracture in elastoplastic hydraulic fracturing.

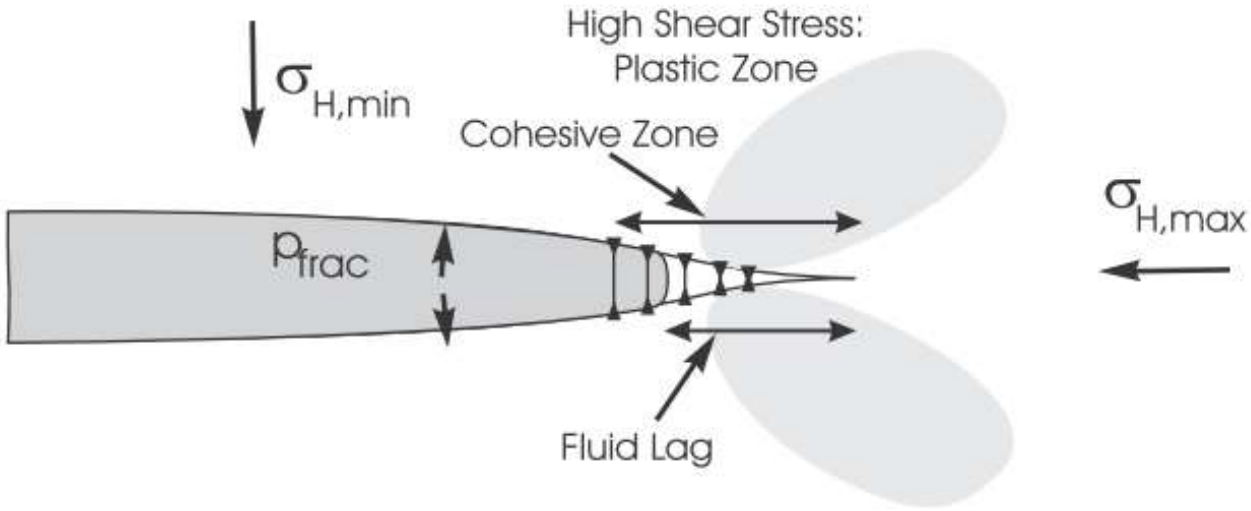

Figure 1.2 Stresses and process zone at a hydraulic fracture tip (Dam *et al*, 2000).

Zhai and Sharma (2005) have modeled hydraulic fracturing in unconsolidated sand without use of LEFM. Instead they studied the pressure diffusion and subsequently, porosity and permeability change due to effective stress change. Therefore the definition of fracture in their study is not the typical mode I (opening tensile mode fracture) but it is defined as the region of enhanced porosity and permeability. Their model includes both the shear and tensile failure. They observed that the volume of the shear enhanced permeability is substantial compared to the volume of the open tensile fracture induced, which is limited to an area just close to the wellbore.

Dean and Schmidt (2009) developed fully coupled a geo-mechanical reservoir simulator that combined hydraulic fracture growth, multiphase/multicomponent Darcy/non-Darcy porous flow, heat convection and conduction, solids deposition, and poroelastic/poroplastic deformation in a single application. The program contained two separate criteria that could be used to model fracture propagation: a critical fracture-opening criterion based on a stress-intensity factor and a cohesive zone model that used quadrilateral cohesive elements in the fracture. The cohesive zone model includes a cohesive strength and an energy release rate in the calculations at the tip of a propagating hydraulic fracture. Simulated fracture lengths without leak-off are compared with analytical solution for both KGD and penny-shaped model, but poroelastic/poroplastic formation behaviors are not investigated in this study.

Vyacheslav Mokryakov (2011) proposed an analytical solution for hydraulic fracture with Barenblatt's cohesive tip zone based on KGD model, by assuming impermeable, elastic rock without considering leak-off. It is also mentioned that derived (cohesive tip zone model) solution can fit the experimental data (pressure log) much more accurately for the case of soft rock fracturing and thus give additional information during interpretation. The relationship between the cohesive parameters and rock limit fracture toughness is also investigated.

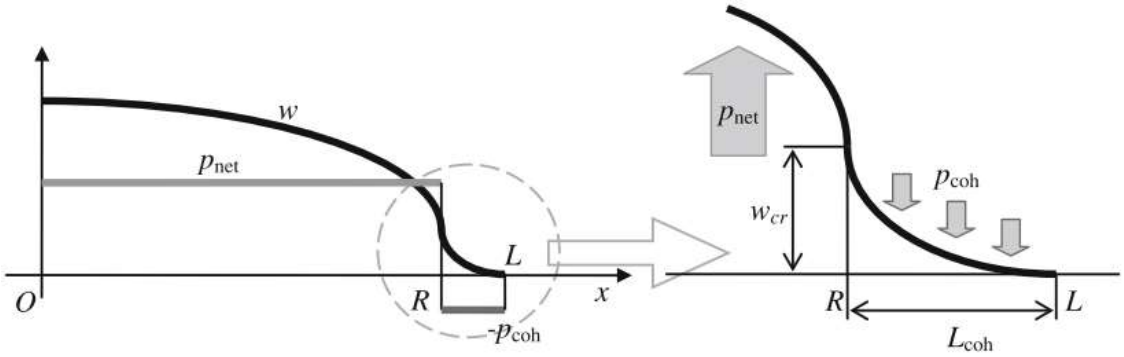

Figure 1.3 In the cohesive zone model, an inviscid fluid has zero pressure drop along the fracture (Vyacheslav, 2011).

E. Sarris et al. (2012) developed a poroelastic cohesive zone method and investigated the effects of permeability, injection rate and formation compressibility on fracture geometry, it is concluded that higher pressures are needed to extend a fracture in a poroelastic medium than in an elastic medium, and the created profiles of poroelastic fracture are wider. A constant permeability of cohesive zone is assumed in this study instead of a rigorous leak off model.

YaoYao (2012) developed a 3D cohesive zone model to predict fracture propagation in brittle and ductile rocks and effective fracture toughness method was proposed to consider the fracture process zone effect on the ductile rock fracture. A theoretical method has been introduced to calculate the effective fracture toughness for quasi-brittle/ductile rocks depends on process zones in defferent material.

The result show that with the increase of fracture toughness, the pore pressure cohesive zone model gives predictions that are more conservative on fracture length as compared with pseudo 3D and PKN models. However, the propagation pressure is not investigated and the leak-off model used in this study is not consistent between cohesive zone model and analytical models.

1.3 Research Objectives

There are three main objectives of this study:

1. Develop a fully coupled numerical model to investigate the impacts of formation plastic behavior on fracture net pressure and geometry.
2. Find out the controlling factors that influence the effects of plastic behavior.
3. Compare the results between poroelastic and poroplastic formation.

1.4 Organization of This Thesis

This thesis tries to capture the differences between the fracture propagation mechanism in hard and soft rocks by taking both poroelatic coupling and plastic deformation effects in to consideration, in addition, the effects of different parameters affecting the fracture mechanism in soft rock formations are also investigated.

- Chapter 2 presents the theoretical background for this study, modeling hydraulic fracture in a fully coupled manner with cohesive zone method.
- Chapter 3 describes the model and all the input parameters.
- Chapter 4 includes the simulations results and analysis for both short term and long term injection.
- Chapter 5 presents the conclusions and recommendations for future work based on the results and observation through this research.

2. MATHEMATICAL MODELING OF HYDRAULIC FRACTURE

The physical process of the fluid driven fracture involves the pumping of a viscous fluid that pressurizes the fracture surfaces which deform. Increasing the pressurization, critical loading conditions will be reached ahead of the tip splitting the rock and driving hydraulically the fracture. Depending on the formation properties, in-situ stresses and pumping parameters, the fracture may propagate for more than hundred meters. The simulation of the HF process is not a trivial task because it involves the coupling of at least four physical mechanisms: (1) the fluid-flow within the fracture, (2) the deformation of the surrounding medium induced by the fluid pressure on the fracture surfaces, (3) the leak-off of the fracturing fluid in the permeable medium, and (4) the fracture propagation.

2.1 Fluid Flow in the Fracture

Rheological characteristics of a fluid determine its response to imposed stresses or inversely, the stresses generated when a fluid moves under imposed deformations or motions. Depending on the response of the fluid under stress, they are classified as Newtonian or non-Newtonian fluids. Newtonian fluids are defined to be those exhibiting a direct proportionality between shear stress and shear rate in laminar flow

$$\tau = \mu \frac{du}{dy}, \tag{2.1}$$

where μ is the viscosity. The simplest rheological model used for non-Newtonian fluids is the power-law model. This model has two constants, namely a power-law index, n, and a consistency index, K, and is written as (Whittaker, 1985)

$$\tau = K\gamma^{n}, \tag{2.2}$$

where γ is the shear rate. If n > 1. the fluid is dilatant; and if n < 1. It is pseudo- plastic.

Most fracturing fluids possess a non-Newtonian behavior and in most applications, the power-law model is used. This is a good assumption for most uncrosslinked gels. In order to avoid additional complexity added by fluid behavior, incompressible and Newtonian fluid is assumed in this study. The continuity equation which imposes the conservation of mass in one dimensional flow is (Boone and Ingraffea 1990)

$$\frac{\mathrm{dq}}{\mathrm{dx}} - \frac{\mathrm{dw}}{\mathrm{dt}} + \mathrm{q_l} = 0\,, \tag{2.3}$$

where q is the local flow rate along the fracture in direction x , $\mathrm{q_l}$ is the local fluid loss in rock formation and w is the crack opening. For a flow between parallel plates, the conservation equation of momentum balance can be used to relate the pressure gradient to the fracture width for a Newtonian fluid of viscosity :

$$q = uw = -\frac{w^3 \mathrm{d}p}{12\mu \mathrm{d}x}\,, \tag{2.4}$$

2.2 Fluid Leak-off

The fluid which leaks from the fracture into the rock formation is referred to as fluid loss. As a first approximation, assuming that the fluid in the fracture has the same viscosity and compressibility as the reservoir fluid, the fluid leak-off is calculated using a one-dimensional steady-state potential flow perpendicular to the fracture wall. This is referred to as Carter's model of leak-off, which is usually written as (Howard and Fast, 1970):

$$\mathrm{v_L} = \frac{\mathrm{C_L}}{\sqrt{\mathrm{t}}} \text{ and} \tag{2.5}$$

$$\frac{\mathrm{V_L}}{\mathrm{A_L}} = 2\mathrm{C_L}\sqrt{\mathrm{t}} + \mathrm{S_p}\,, \tag{2.6}$$

where v_L is leak-off velocity, C_L is leak-off coefficient, t is the time elapsed since the start of the leakoff process, V_L is the fluid volume that passes though the surface A_L during the time period from time zero to time t, the integration constant S_p is called spurt loss. The two coefficients C_L and S_p, can be determined from laboratory tests.

2.3 Flow in Porous Medium

For the movement of the fluid in the porous skeleton, with respect to the solid, it is assumed that the diffusion of pore fluid obeys the Darcy law. This classical transport law for isotropic, porous media relates q to the gradient of the fluid pressure p according to Equation (2.7) as follows:

$$\mathrm{q} = -\frac{\mathrm{k}}{\mu}(\nabla \mathrm{p} - \mathbf{f}), \tag{2.7}$$

where q is fluid flux velocity in the porous media, k is tensor permeability, ∇p is formation pressure gradient and **f** are the fluid volume forces.

2.3 Poroelasticity

The poroelasticity theory is a macroscopic continuum mechanics approach with the stress strain relations defined over a uniform and homogenized region which is large enough to include a large number of grains and pores. Using the convention that a positive stress implies tension and positive strain implies extension, and denoting the total stress tensor by σ and the strain tensor by ε , the constitutive relations for an isotropic solid are (Jaeger et al., 2007)

$$\boldsymbol{\sigma} + \alpha p\mathbf{I} = 2\mathrm{G}\boldsymbol{\varepsilon} + \frac{2G\nu}{1-2\nu} trace(\boldsymbol{\varepsilon})\mathbf{I}\,, \tag{2.8}$$

where

G = the shear modulus,

υ = the drained Poisson's ratio,

$\alpha = 1 - \frac{K}{K_m}$, is the Biot's effective stress coefficient,

K = drained bulk modulus,

K_m = bulk modulus of solid matrix,

$trace(\boldsymbol{\varepsilon}) = \varepsilon_{xx} + \varepsilon_{yy} + \varepsilon_{zz}$ is the bulk volumetric strain, and

I = identity matrix.

The strains are related to the displacements according to the compatibility relations:

$$\boldsymbol{\varepsilon} = \frac{1}{2}(\nabla \boldsymbol{u} + (\nabla \boldsymbol{u})^T). \tag{2.9}$$

The equilibrium equations are

$$\nabla . \boldsymbol{\sigma} = -\mathbf{F}\,, \tag{2.10}$$

where **F** is the body force vector per unit volume of the bulk material. The constitutive equation for the pore fluid is:

$$p = \mathrm{M}(\zeta - \alpha \varepsilon_b), \tag{2.11}$$

where

ζ = variation of fluid volume per unit volume of the porous material,

$M = \frac{K_u - K}{\alpha^2}$, is the Biot modulus,

K_u = undrained bulk modulus, and

ε_b = bulk volumetric strain.

The continuity equation for the fluid phase is

$$\frac{\partial \zeta}{\partial \mathrm{t}} + \nabla . \boldsymbol{q} = 0\,. \tag{2.12}$$

Finally Darcy's law states

$$\mathrm{q} = -\frac{\mathbf{k}}{\mu}\left(\nabla \mathrm{p} - \rho_f \mathbf{g}.\mathbf{x}\right), \tag{2.13}$$

where

g = gravitational acceleration vector,

x = position vector.

The above equations can be reduced by substitution and elimination into a Nervier type equation for the displacements and a diffusion type equation for the pore pressure, both containing a coupling term. The Nervier-type equation for the displacements is (Detournay and Cheng 1993)

$$\mathrm{G}\nabla^2\mathbf{u} + \frac{G}{1-2\upsilon}\nabla(\nabla.\mathbf{u}) = \alpha\nabla p - \boldsymbol{F}. \tag{2.14}$$

The coupling term $\alpha\nabla p$ in the above equation may be seen as an additional body force proportional to the gradient of the pore pressure. The diffusion equation for p for a uniform homogenous porous material is

$$\frac{\partial \mathrm{p}}{\partial \mathrm{t}} - \frac{\boldsymbol{k}}{\mu}M\nabla^2 p = -\alpha M\frac{\partial \varepsilon_b}{\partial \mathrm{t}} - \frac{\boldsymbol{k}}{\mu}M\nabla^2\left(\rho_f \mathbf{g}.\mathbf{x}\right). \tag{2.15}$$

Here again the coupling term proportional to the rate of change of volumetric strain $-\alpha M\frac{\partial \varepsilon_b}{\partial \mathrm{t}}$ can be seen as an additional external force or a source term driving the pressure distribution. Given appropriate initial and boundary conditions over the domain of interest, the coupled equations (2.14) and (2.15) can be solved for the displacement vector u and the pressure field p in space and time. More detailed treatment can be found in Detournay and Cheng (1993) and Jaeger et al. (2007).

2.4 Plastic Yield

The Mohr-Coulomb plasticity model is implemented for modeling elasto-plastic behavior of rock, where there is a regime of purely linear elastic response, after which some of the material deformation is not recoverable. The elastoplastic material behavior of formation is modeled by writing the constitutive equations in incremental form.

2.5 Fracture Initiation and Propagation

In examining the plentiful literature concerning fracture mechanics the cohesive zone modeling has been adopted by many authors to model fracture initiation and propagation. The cohesive zone is a region ahead of the crack tip that is characterized by microcracking along the crack path. The main fracture is formed by inter connection of these micro cracks. The idea of a cohesive zone appeared from attempts to resolve the tip singularity contradiction predicted by LEFM. The constitutive behavior of the cohesive zone is defined by the traction-separation relation derived from laboratory tests. The traction-separation law for the surface is such that with increasing separation, the traction across this cohesive surface reaches a peak value and then decreases and eventually vanishes, permitting for a complete separation. A cohesive potential function $\emptyset$ is defined so that the traction is given by

$$\mathrm{T} = \frac{\partial \emptyset}{\partial \delta}, \tag{2.26}$$

where T is traction force and δ is the displacement across a pair of cohesive surface. Various types of traction-separation relations (potential functions) for cohesive surfaces have been proposed to simulate the fracture process in different types of material systems.

This law assumes that the cohesive surfaces are intact without any relative displacement and exhibit reversible linear elastic behavior until the traction reaches the cohesive strength T_{Max} (tensile strength) or equivalently the separation exceeds the displacement of damage initiation, δ_0. Beyond δ_0, the traction reduces linearly to zero up to the displacement of complete failure δ_f, and any unloading takes place irreversibly. For mode-I plane strain, the area under the traction-separation curve equals the fracture energy G_{IC}, which is the work needed to create a unit area of fully developed crack. For elastic solids this energy is related to the rock fracture toughness K_{IC} through (Rice 1968; Kanninen and Popelar1985):

$$G_{IC} = \frac{K_{IC}^{\,2}}{E}\left(1 - \nu^{2}\right), \tag{2.27}$$

where E is Young's modulus of formation and ν is Poisson's ratio. For bilinear traction-separation law, displacement of complete failure δ_f can be determined by:

$$\delta_f = \frac{2\,G_{IC}}{T_{Max}} = \frac{2K_{IC}^{\,2}\left(1 - \nu^{2}\right)}{ET_{Max}}. \tag{2.28}$$

The stress-displacement relation in the initial part of the loading curve corresponds to linear elastic deformation as follows:

$$\sigma = \frac{\delta T_{Max}}{\delta_0} = \delta K_n, \tag{2.29}$$

where K_n is the stiffness of the stress-displacement relation in the loading regime and is assumed to be equivalent to the stiffness of formation in this study according to the following equation:

$$\sigma = \delta K_n = \frac{E\delta}{d}, \tag{2.30}$$

where d is the initial thickness of cohesive surfaces and the post-peak softening regime the deformation is given by the following:

$$\sigma = T_{Max}\left[1 - \frac{(\delta - \delta_0)}{(\delta_f - \delta_0)}\right]. \tag{2.31}$$

In order to guarantee solution convergence, and to properly capture the details of the deformation field in the vicinity of the crack tip and the traction distribution within the cohesive zone, the cohesive element size must be smaller than the cohesive zone length. The cohesive zone length is an inherent length scale determined by material properties. For mode-I crack growth under plane strain conditions, the cohesive zone length d_z is determined by:

$$d_z = \frac{9\pi {K_{IC}}^2}{32 {T_{Max}}^2} = \frac{9\pi E G_{IC}}{32(1-\nu^2){T_{Max}}^2}\,. \tag{2.32}$$

Conventional hydraulic fracture models treat the fracture as a mode I fracture, which is compatible with the field and lab observations for hard rock formations, however, it is not sufficient when a pronounced shear stress component exists. Mode II type fracture can play an important role under certain loading conditions in rock fracture mechanics.

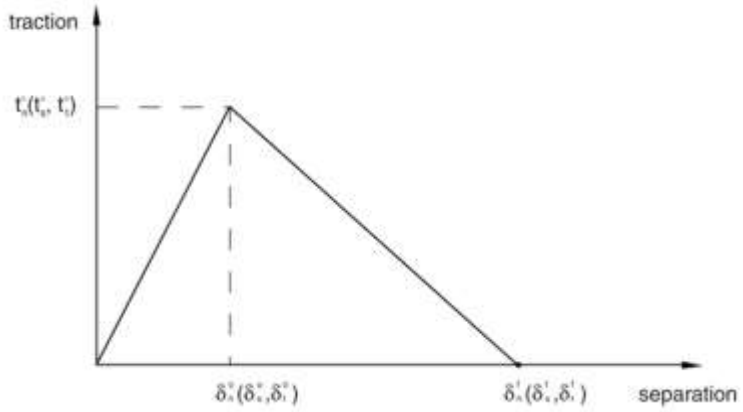

Figure 2.1 Traction-separation response

The Traction-Separation Law presented for Mode-I-based fracture criteria can be easily extended to mixed-mode fracture criteria. For an isotropic formation, the traction-separation responses in different modes are assumed to be the same, as shown in Fig. 2.1. where t_n, t_s, t_t refer to the nomal, the first, and the second shear stress components; and t_n^0, t_s^0, t_t^0 represent the peak values of the nominal stress when the deformation is either purely normal to the interface or in the first or the second shear direction; $\delta_n^0, \delta_s^0, \delta_t^0$ corespond to the displacement of initial damage in the normal, the first, and the second shear stress direction and $\delta_n^f, \delta_s^f, \delta_t^f$ are the displacement of complete failure in these there directions.

The elastic behavior can then be written as

$$\mathbf{t} = \begin{Bmatrix} t_n \\ t_s \\ t_t \end{Bmatrix} = \begin{bmatrix} K_{nn} & K_{ns} & K_{nt} \\ K_{ns} & K_{ss} & K_{st} \\ K_{nt} & K_{st} & K_{tt} \end{bmatrix} \begin{Bmatrix} \varepsilon_n \\ \varepsilon_s \\ \varepsilon_t \end{Bmatrix} = \mathbf{K\varepsilon}\,, \tag{2.33}$$

where **K** is the elasticity matrix. The elasticity matrix provides fully coupled behavior between all components of the traction vector and separation vector. Set the off-diagonal terms in the elasticity matrix to zero if uncoupled behavior between the normal and shear components is desired. In this study, we assume no coupling effects between the normal and shear stress, which is then

$$\mathbf{t} = \begin{Bmatrix} t_n \\ t_s \\ t_t \end{Bmatrix} = \begin{bmatrix} K_{nn} & & \\ & K_{ss} & \\ & & K_{tt} \end{bmatrix} \begin{Bmatrix} \varepsilon_n \\ \varepsilon_s \\ \varepsilon_t \end{Bmatrix}\,. \tag{2.34}$$

The initial response of the cohesive element is assumed to be linear as discussed above. However, once a damage initiation criterion is met, material damage can occur according to a damage evolution law. Damage initiation refers to the beginning of degradation of the response of a material point. The process of degradation begins when the

stresses and/or strains satisfy certain damage initiation criteria. In this study, Damage is assumed to initiate when a quadratic interaction function involving the nominal stress ratios reaches a value of one. This criterion can be represented as

$$\left\{\frac{\langle t_n \rangle}{t_n^0}\right\}^2 + \left\{\frac{t_s}{t_s^0}\right\}^2 + \left\{\frac{t_t}{t_t^0}\right\}^2 = 1 \,. \tag{2.35}$$

The symbol ⟨ ⟩ used in the above equation represents the Macaulay bracket with the usual interpretation. The Macaulay brackets are used to signify that a pure compressive deformation or stress state does not initiate damage.There are two components to the definition of the evolution of damage. The first component involves specifying the energy dissipated due to failure G^c , The area under the stress-displacement curve, Fig.2.2. The second component to the definition of damage evolution is the specification of the nature of the evolution of the damage variable, D, between initiation of damage and final failure.

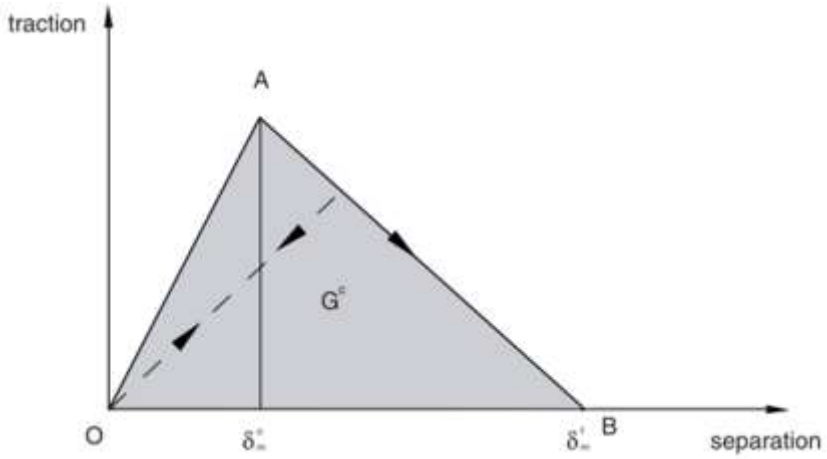

Figure 2.2 Linear damage evolution for mix-modes

The scalar damage variable, D, represents the overall damage in the material and captures the combined effects of all the active mechanisms. It initially has a value of 0. If damage evolution is modeled, D monotonically evolves from 0 to 1 upon further loading

after the initiation of damage. The stress components of the traction-separation model are affected by the damage according to

$$\mathbf{t} = \begin{cases} (1-D)\bar{\boldsymbol{t}} & \text{damage initated} \\ \bar{\boldsymbol{t}}, & \text{no damage occurs} \end{cases} . \tag{2.36}$$

$\bar{\boldsymbol{t}}$ are the stress components predicted by the elastic traction-separation behavior for the current strains without damage. To describe the evolution of damage under a combination of normal and shear deformation across the interface, it is useful to introduce an effective displacement (Camanho and Davila, 2002) defined as

$$\delta_m = \sqrt{\langle \delta_n \rangle^2 + \delta_s^2 + \delta_t^2} . \tag{2.36}$$

For linear softening (see Figure 2.7), the evolution of the damage variable, D, that reduces to (Turon et al., 2006)

$$\mathrm{D} = \frac{\delta_m^f (\delta_m^{max} - \delta_m^0)}{\delta_m^{max} (\delta_m^f - \delta_m^0)} . \tag{2.37}$$

The mode mix of the deformation fields in the cohesive zone quantify the relative proportions of normal and shear deformation. The damage evolution for mixed-mode failure in the current model is defined based on the Benzeggagh–Kenane fracture criterion (Benzeggagh and Kenane 1996), when the critical fracture energies during deformation along the first and the second shear directions are similar.

$$\mathrm{G^c} = \mathrm{G_n^c} + (\mathrm{G_s^c} - \mathrm{G_n^c})\left(\frac{\mathrm{G_{shear}}}{\mathrm{G_{total}}}\right)^{\eta} , \tag{2.38}$$

where $\mathrm{G_{shear}} = \mathrm{G_s^c} + \mathrm{G_t^c}$, $\mathrm{G_{total}} = \mathrm{G_{shear}} + \mathrm{G_n^c}$. $\mathrm{G_n^c}, \mathrm{G_s^c}, \mathrm{G_t^c}$ are the work done by the tractions and their conjugate relative displacements in the normal, first, and second shear directions.

3. SIMULATION MODEL

3.1 Model Description

Following fracture initiation, further fluid injection results in fracture propagation. Based on classical models, biwing fractures are created and the geometry of the created fracture can be approximated by taking into account the mechanical properties of the rock, the properties of the fracturing fluid, the conditions with which the fluid is injected (rate, pressure), and the stresses and stress distribution in the porous medium.

There general families of models are available in describing fracture propagation: two-dimensional (2D), pseudo-three-dimensional (P-3D) and, fully three-dimensional (3D). The latter allow full three-dimensional fracture propagation with full two-dimensional fluid flow; the fracture is allowed to propagate laterally and vertically.

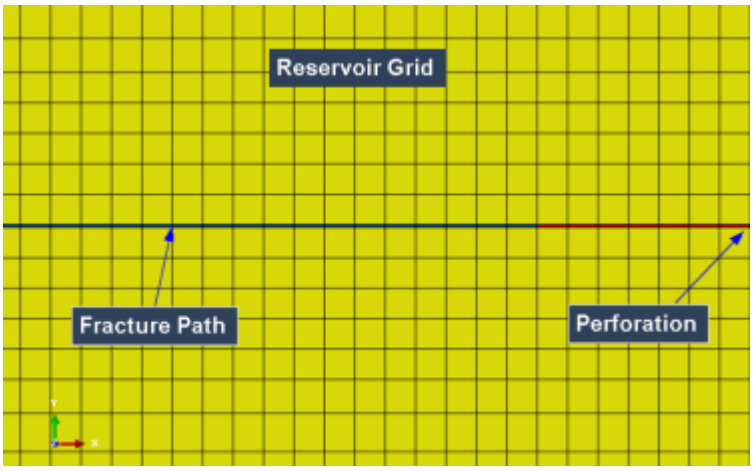

Figure 3.1 Reservoir and fracture grid around fracture path.

A two dimensional plane strain fluid-driven fracture in porous rock is simulated, as shown in Fig.3.1. The initially unopened fracture is represented by an embedded array of cohesive zone elements without initial separation along the entire fracture path. Four-node,

plain strain, isoparametric elements were used to model the domain and six-node cohesive elements to model the fluid-flow in the fracture and the fracturing process. Both types of elements, additionally from their pressure, displacement translation degree of freedom are equipped with a pore-pressure degree of freedom to account for the fluid saturation in the domain. A one-to-one correspondence exists between the plain strain flow and domain elements at the corner nodes along the fracture path, ensuring that the fluid mass is conserved across their interface. The two additional nodes in the cohesive elements, positioned in their center, are used to simulate the fluid-flow during the propagation. An incompressible Newtonian fluid is injected at a constant rate. The cohesive elements at the injection point are defined as initially open as perforation tunnel to allow entry of the fluid, so that the initial flow and fracture growth are possible. Grid size along the fracture path is 0.2 m and all the outer boundaries of this model are fixed. No special remeshing scheme was used because the mesh was defined to be sufficiently fine along the fracture.

The inelastic rock material behavior follows the Mohr-Coulomb flow theory of plasticity for a cohesive frictional dilatant material. Associative behavior with constant dilatation angle is considered. These assumptions are justified by the presence of high confining stresses prior to crack propagation and to a decrease in the initial in-situ mean pressure near the crack tip during propagation. There different types of formation were investigated, which are poroelastic formation, poroelastic formation with increased effective toughness and poroplastic formation. For typical quasi-brittle materials, the effective toughness can be 1.141 to 2.236 times higher than original toughness, and for ductile rock, the effective toughness can be determined by investigating softening behavior experimentally or computationally (YaoYao 2012). The effective toughness is assumed to

be 3 times higher than the original toughness in this study and the stress-strain curve was adjusted for formations with different plastic behavior. The cohesion yield strength of 3 types of formations are 2 MPa, 4 MPa and 6 MPa respectively, which represent formations with relative low, moderate and high yield strength in this study. Low cohesion yield strength can be explained by weakly cemented formation grains, the presence of microfractures and other planes of weaknesses, or by reactivation of pre-existing, sealed natural fractures. All the other input parameters are shown in Table.3.1 unless otherwise specified.

Table 3-1 Input Parameters

Elastic Modulus, Gpa	20
Poisson's Ratio	0.25
Fluid viscosity, cp	1
Tensile strength, Mpa	2
Formation Permeability, md	10
Flow rate Q (m^3/s/unit height)	0.0005
Specific Weight of Fluid, kN/m^3	9.8
Initial Pore Pressure, Mpa	20
Maximum Horizontal Stress, Mpa	42
Minimum Horizontal Stress, Mpa	37
Vertical Stress, Mpa	70
Fracture Toughness , Mpa$\sqrt{m}$	1
Carter's Leakoff Coefficient, m/$\sqrt{s}$	2.00E-06
Spurt Loss Coefficient, m	2.5E-04
Porosity	0.2
Friction angle	27°
Dilation angle	8°

3.2 Numerical Implementation

The theory of poroelasticity can be approximated numerically by using the finite element method and a standard Galerkin formulation as described by Zienkiewicz (1984) and Lewis and Schreffler (2000). Governing equations are discretized in space by the finite element method and in time by the finite difference method. The generalized discrete finite

element equations that also account for transient behavior are described hereafter at the element level. Adopting the Lewis and Schreffler (2000) notation, the final equations yield the following:

$$\begin{bmatrix} \theta \mathbf{K_e} & \theta \mathbf{Q} \\ \mathbf{Q^T} & \mathbf{S} + dt\theta \mathbf{H} \end{bmatrix}_{n+\theta} \begin{Bmatrix} \overline{\mathbf{u}} \\ \overline{\mathbf{p}}^f \end{Bmatrix}_{n+1} =$$

$$\begin{bmatrix} (\theta - 1)\mathbf{K_e} & (1-\theta)\mathbf{Q} \\ \mathbf{Q^T} & \mathbf{S} - (1-\theta)dt\mathbf{H} \end{bmatrix}_{n+\theta} \begin{Bmatrix} \overline{\mathbf{u}} \\ \overline{\mathbf{p}}^f \end{Bmatrix}_{n} + \begin{Bmatrix} \mathbf{f}^u \\ dt\mathbf{f}^p \end{Bmatrix}_{n+\theta}, \tag{3.1}$$

where, $\mathbf{K_e}$ = elastic stiffness matrix; $\mathbf{Q}$ = coupling matrix; $\mathbf{H}$ = permeability matrix, $\mathbf{S}$ = compressibility matrix; $\mathbf{f}^u$ = forces resulting from displacements; and $\mathbf{f}^p$ = forces resulting from pressures. θ , is the time operator that defines the type of numerical method used to approximate the time in the equations, $0 \leqslant \theta \leqslant 1$. Eq. (3.1) can be decomposed into the following matrices to account for both, stiffness and flow equations:

$$\mathbf{B} = \mathbf{L}\mathbf{N_u} \text{ (Strain Operator)}, \tag{3.2}$$

$$\mathbf{K_e} = \int_\Omega \mathbf{B}^{\boldsymbol{T}} \mathbf{D_e} \boldsymbol{B} d\Omega \text{ (Linear Elastic Stiffness Matrix)}, \tag{3.3}$$

$$\mathbf{Q} = \int_\Omega \mathbf{B}^{\boldsymbol{T}} \alpha m \mathbf{N_p} \mathrm{d}\Omega \text{ (Coupling matrix)}, \tag{3.4}$$

$$\mathbf{H} = \int_\Omega (\nabla \mathbf{N_p})^{\mathrm{T}} \frac{k}{\mu} \nabla \boldsymbol{N_p} d\Omega \text{ (Permeability matrix)}, \tag{3.5}$$

$$\mathbf{S} = \int_\Omega \mathbf{N_p}^{\mathrm{T}} (\frac{1}{Q'}) \boldsymbol{N_p} d\Omega \text{ (Compressiblity matrix)}, \tag{3.6}$$

$$\frac{1}{Q'} = \frac{\alpha - n}{K_s} + \frac{n}{K_f}, \tag{3.7}$$

$$f^u = \int_\Omega \boldsymbol{N_u}^{\boldsymbol{T}} [\rho^s (n-1) + \rho^f n] g d\Omega + \int_{\Gamma_u^q} \mathbf{N_u}^{\mathrm{T}} \bar{t} d\Gamma \text{ , and} \tag{3.8}$$

$$f^p = \int_\Omega (\nabla \boldsymbol{N_p})^{\mathrm{T}} \frac{\boldsymbol{k}}{\mu} \rho^f g d\Omega - \int_{\Gamma_w^q} \mathrm{N_p}^{T} \frac{q^f}{\rho^f} d\Gamma \text{ ,} \tag{3.9}$$

where $\mathbf{N_u}$, $\mathbf{N_p}$ as the shape functions to account for the displacements and fluid pressures, respectively; **L** = differential operator; $\mathbf{D_e}$ = tangential elastic stiffness matrix; n = porosity of the solid phase; ρ^f = density of the fluid; μ = viscosity of the fluid; $\boldsymbol{K_s}$ and $\boldsymbol{K_f}$ = solid and fluid bulk modulus, respectively; and finally, **k** = intrinsic permeability.

For the numerical approximation of the aforementioned set of equations, Newton-Raphson technique was used to solve the coupled equations, The primary variables of the system are the fluid pressures in the reservoir, the fluid pressures in the fracture (or fluid volumes in the fracture if partially saturated), and the well pressure. Because a fracture may grow or contract during a time step, the fracture solution for a time step is computed through use of a three-step process:

1. The first step assumes that the fracture boundaries are fixed and the system of equations is solved for the given fracture configuration (a fracture may open wider or become narrower, but the edges of the fracture do not change). The system of equations is solved by use of a Newton-Raphson technique in which the Jacobian is generated for the entire system of equations and incremental corrections are found by use of a linear solver that includes all the solution variables. The program generates the Jacobian for the full system to increase robustness and to preserve second-order convergence for the nonlinear iterations.

2. After the solution has converged for the given fracture geometry, the program then uses one of the propagation criteria described above to determine if the fracture edges move and checks the displacement solution to see if portions of the fracture surface have closed. If no changes are detected in the boundaries, then the program goes on to the next time step; otherwise, the program proceeds to step 3 and then starts over at step 1 with the

new fracture boundaries. This process continues until no additional changes occur in the fracture boundaries for that time step.

3. If the propagation criteria are exceeded and the fracture grows, then displacement constraints are removed at the appropriate boundary nodes and the fracture is allowed to open at those points and the fluid pressure in the fracture becomes a traction condition at the newly created fracture surfaces. If the fracture shrinks (i.e., the surface displacements predict a negative fracture width) then the displacement constraints are re-applied at those nodes.

The program for numerical calculations were developed in FORTRAN and finite element code ABAQUS. Two injection cases for both short time and long time treatment were simulated. In the first case, 2 minutes injection and fall off was simulated and the fracture propagated long enough to allow analysis of the results and reach conclusions for long fractures. In the second case, 30 minutes injection was simulated and the results can provide a direct insight of how the fracture geometry and fluid efficiency will be different in a more realistic situation if plasticity is considered.

4. SIMULATION RESULTS AND ANALYSIS

In this section we present results and analysis of the simulation to demonstrate the importance of the plasticity in modeling hydraulic fracturing in soft/unconsolidated formations for both short term and long tern injections. The fracture propagation geometry and fracturing net pressure under different conditions are simulated. In addition, the main factors that affect the poroelastic backstress and the effects of formation plasticity on hydraulic fracture are also investigated.

4.1 Model Validation

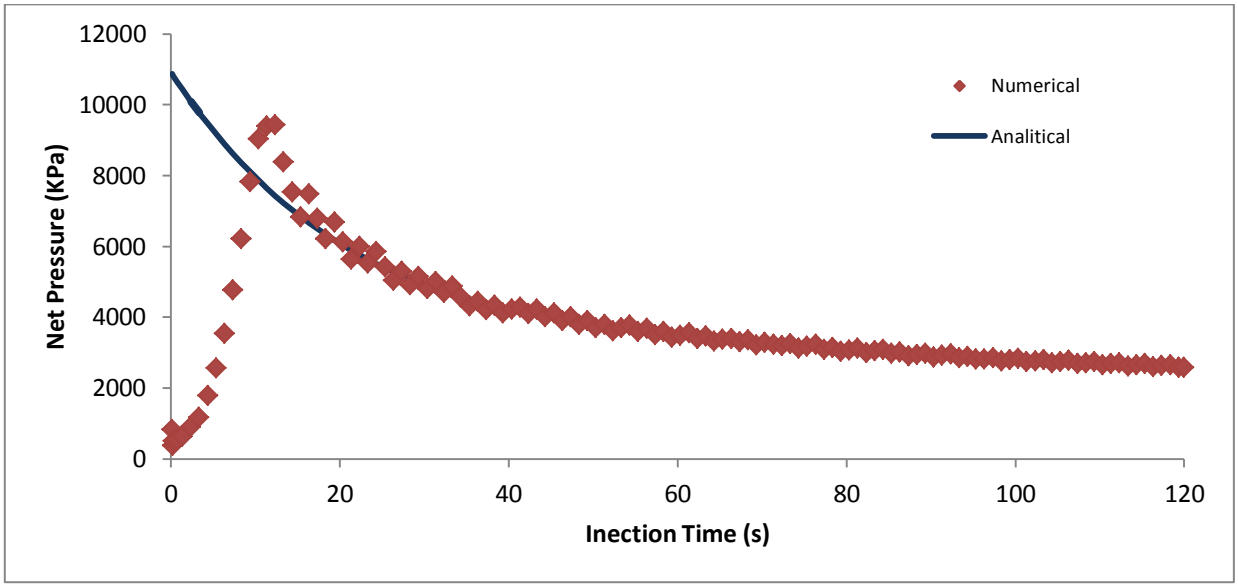

Figure 4.1 Numerical and analytical net pressure at well bore.

In order to examine the accuracy of this model in simulating hydraulic fracture propagation in porous medium, the numerical results were compared with the analytical solution of a 2-D KGD plane-strain tensile fracture model. The analytical solution is given in previous chapter. Because it is not possible to find the analytical solution for the fluid

diffusion and mechanical process, so the comparison to the analytical solution given only for non-coupling effect. To eliminate the poroelasticity effect, Biot's constant is set to be zero by equating the bulk modulus and the grain modulus. All the input parameters are shown in Table3.1. The comparisons between the analytical and numerical solutions are shown in Figure 4.1 and Figure 4.2

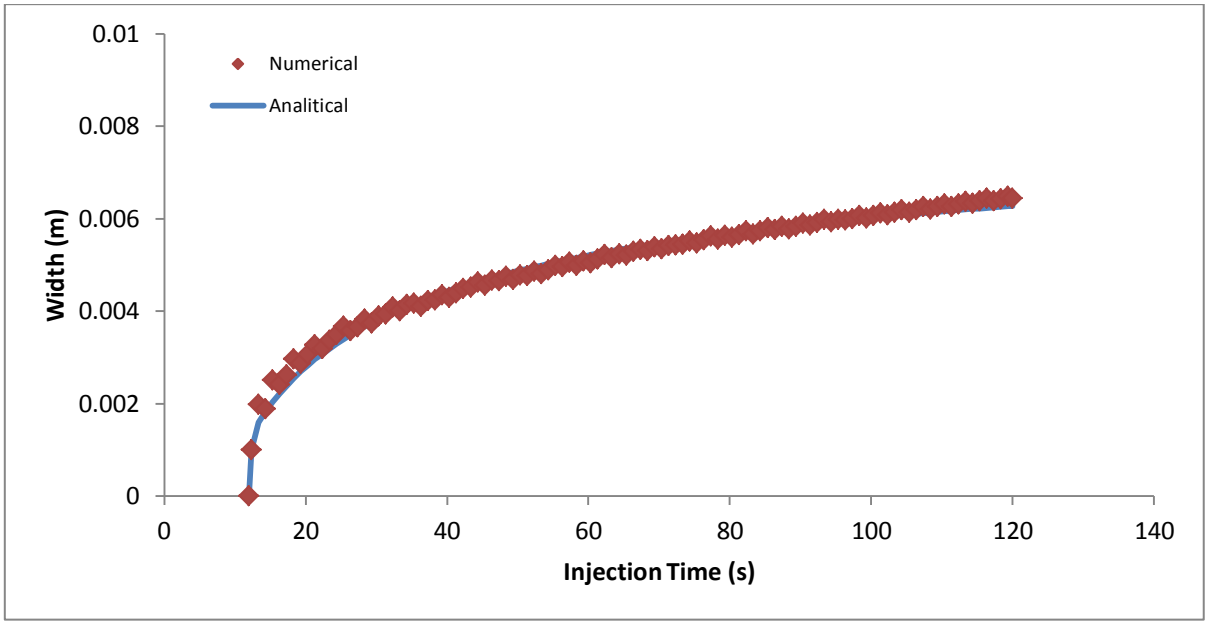

Figure 4.2 Numerical and analytical fracture width at wellbore.

The comparison indicates that the simulation results of this model match the analytical solution very well, except for the net pressure in the early stage of injection; this is because the analytical solution does not account for the period before breakdown. It also should be mentioned that the numerical model is quite sensitive to the mesh size along the fracture. A perfect match between the analytical and numerical solution requires the mesh size to be substantially refined.

4.2 Short Term Injection and Fall-off

In the first case of 2 minutes injection, fracture propagation and fall off were simulated for both elastic and plastic formations. Fig.4.3 demonstrates the relationship between net pressure and fracture width at the wellbore as a function of time. All the input parameters are from Table.3.1 and no plastic properties are included.

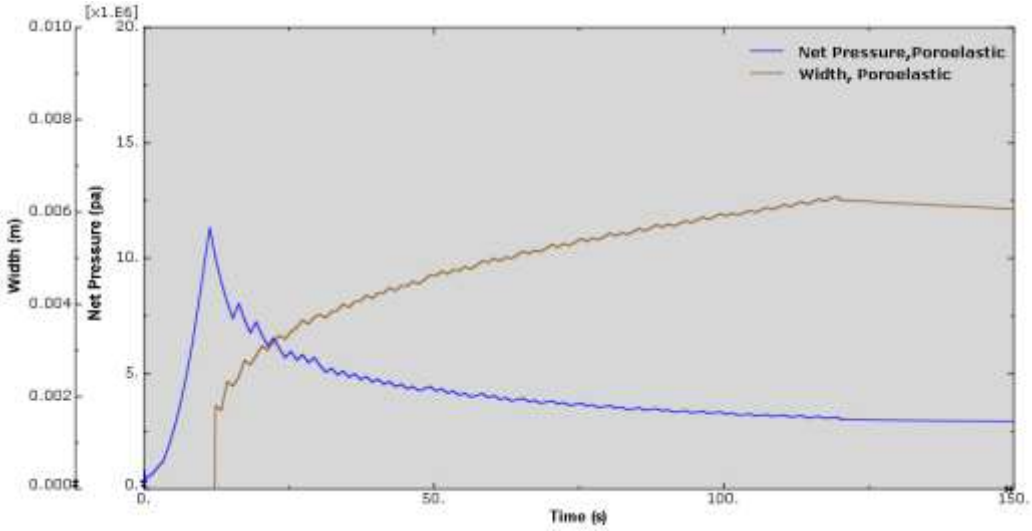

Figure 4.3 Net pressure and width at wellbore in elastic formation during injection.

From Fig.4.3 we can see that after the start of injection, the net pressure increases to a peak point and then decreases continuously as fracture propagation, this is a typical pressure trends in KGD model which indicates the fracture height is not contained by stress barrier and fracture length is shorter than fracture height. When the net pressure reaches the breakdown pressure, which is often much higher than fracture propagation pressure, the fracture initiated and fracture width increases as fracture propagating.

The oscillation of the simulation curve corresponds to halt and sequel in the fracture propagation process step by step for serious of time increments. The pressure drops when new fracture volume created and sudden spurt loss through newly created surface, and then

pressure increases until the cohesive element in front of fracture tip was damaged and new fracture volume was created.

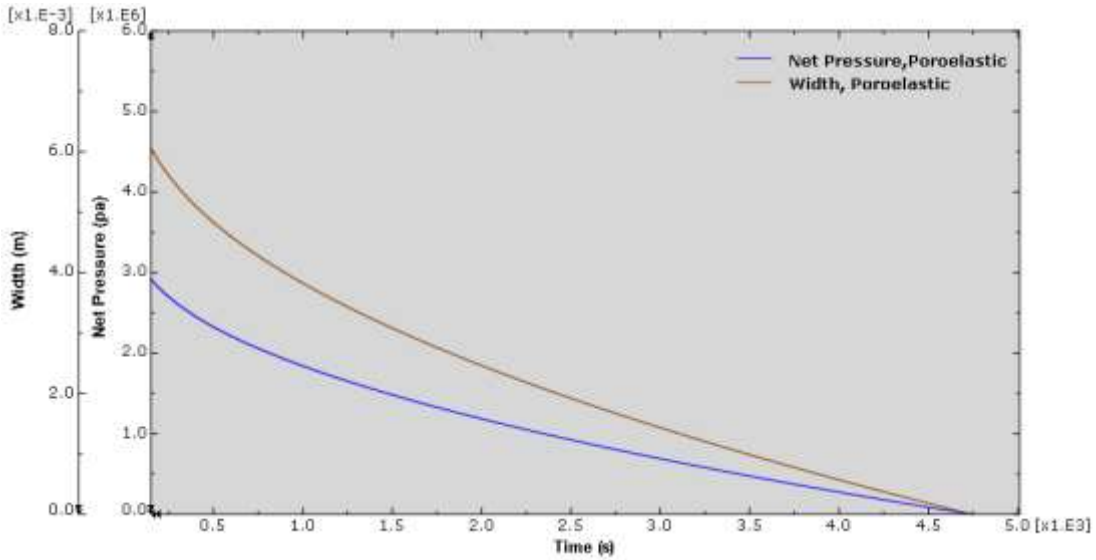

Figure 4.4 Net pressure and width at wellbore in elastic formation during injection.

Fig.4.4 shows the net pressure and maximum fracture width during the fall-off process in elastic formation. As pump stops inject fluid into the fracture after 2 minutes of treatment, the fluid inside the fracture continues leaking off into to the formation slowly, so with less and less fluid remains in the fracture, the pressure inside the fracture decreases and so does the net pressure. Fracture volume also shrinks and the fracture closes (fracture width at the wellbore drops to zero) as the net pressure approaches to zero.

The Carter's Leak-off model was implemented in the simulation as discussed in previous chapter, The cumulative leak-off volume through per cohesive element surface (0.2m) based on was shown in Fig. 4.5, the element was chosen at the wellbore and as we can see, there's a sudden leak-off at the moment of element damage when new fracture surface are created and exposure to injection fluid, then the filtrate cake was build up and

the leak-off rate continues decreasing and the thickness of filtrate cake increases. Overall, the curve of cumulative leak-off volume indicates a relative low leak-off rate, so the fracture will propagate relative longer in a short treatment.

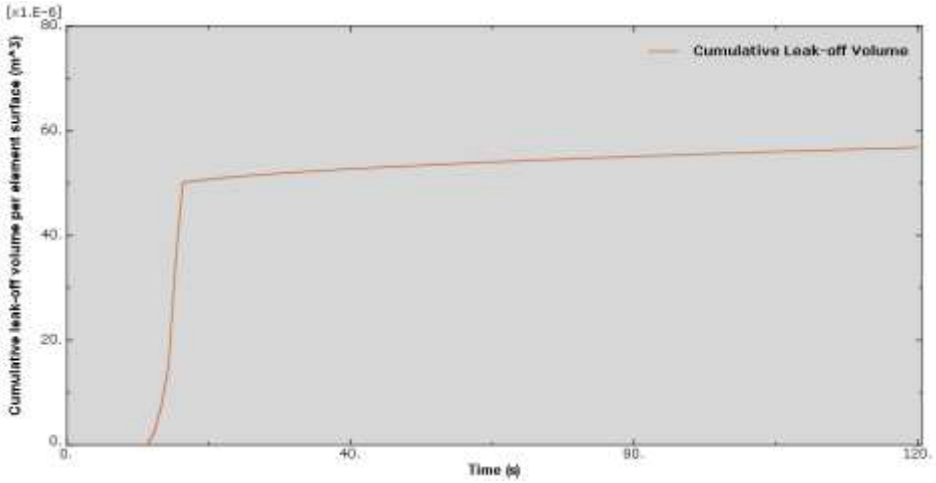

Figure 4.5 Cumulative leak-off volume through per element surface.

Next, two minutes injection and fall-off process was simulated for plastic formation, all the input parameters remains as the same as elastic formation, except for that the plastic yield behavior was added to formation. By comparing the results of the simulation, we can investigate how plasticity can influence fracture geometry and net pressure.

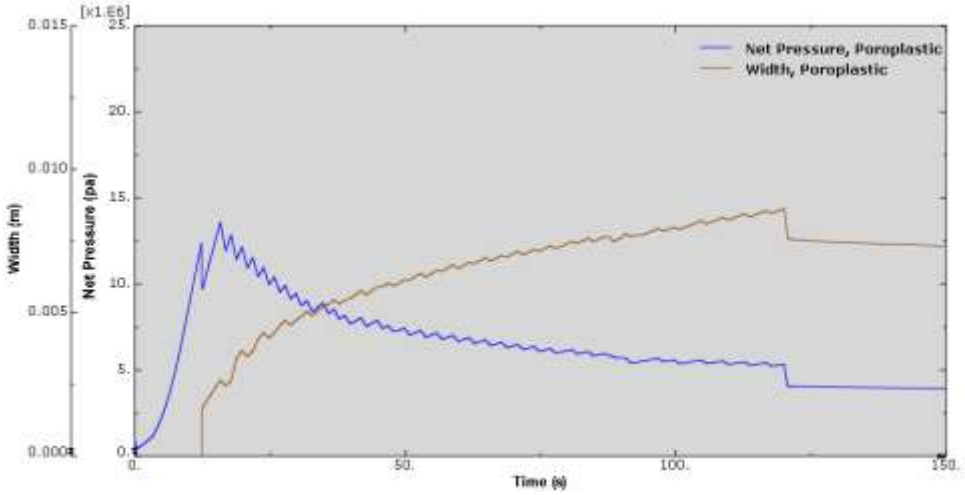

Figure 4.6 Net pressure and width at wellbore in plastic formation during injection.

Fig.4.6 shows the net pressure and maximum fracture width during the fall-off process in plastic formation. The results also follow the general trend of typical KGD model, net pressure decreases after break down and fracture width increase before pump shuts down. Compared with the results in the elastic formation, it can be noted that the net pressure in plastic formation is nearly 2 Mpa higher than that in elastic formation, and the fracture width at wellbore in plastic formation is wider that that in elastic formation after 2 minutes of injection. So in comparison to elastic rock, plastic formations require higher pressure to propagate the fracture under the same treatment conditions and wider fracture tends to be created in plastic formation.

It can also be noted at the moment when the pump stops, there is a larger instant pressure drop in the plastic formation when compared with elastic formation, and also a sudden decrease in fracture width can be observed corresponding to that instant pressure drop. This can be explained by the fact that the energy absorbs by rock deformation in plastic formation will not release as much as elastic formation to compensate fluid pressure drop instantly after shut in.

Fig.4.7 shows the net pressure and maximum fracture width during the fall-off process in plastic formation. The fracture width and net pressure continues to decrease as expected as fluid inside the fracture seeps into the surrounding porous formation. It can be noted that it takes a longer time for the net pressure to drop to zero than that in elastic formation. This comes from the fact that with the same leak-off model and injection rate in both elastic and plastic formation, the fracture is wider in plastic formation. This leads to

shorter fracture length according to material balance, and hence less leak-off surface, which can results larger fracture volume in plastic formation.

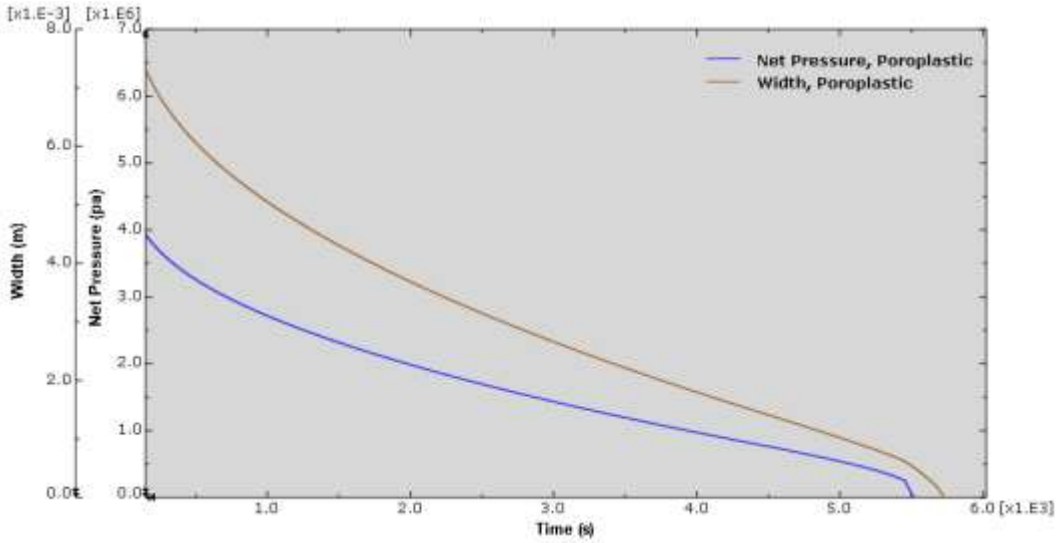

Figure 4.7 Net pressure and width at wellbore in plastic formation during fall off.

It should be also noted that when the net pressure drop to zero, the fracture is still open at the wellbore, this can be explained by that some portion of the rock along fracture path will not return to original state in the unloading process because of permanent plastic deformation. It also suggests that the fracture will close completely at negative net-pressures (fluid pressure less than the far field stress). Application of classical analysis which assumes that the fracture closes completely when the fluid-pressure drops to the value of the far-field stress, would lead to the underestimation of the minimum in-situ stress.

As discussed in previous chapter, the plastic yielding near the tip of a propagating fracture provides an effective shielding, which results in increased toughness. The conception of effective toughness was used by many authors to handle plasticity. With this method, the elastic model of hydraulic fracture can be modified by replacing its origin

toughness with the increased effective toughness, calculated numerically or determined by experiments, to account for the effect of plasticity.

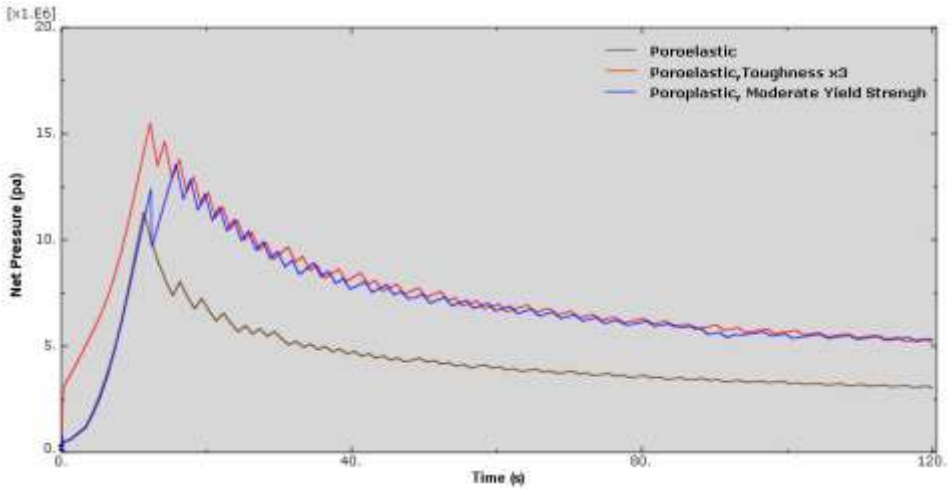

Figure 4.8 Net pressure at wellbore in elastic and plastic formations.

In this study, the original toughness of elastic formation is 1 Mpa$\sqrt{m}$, the cohesion yield strength of moderate plastic formation is 4 MPa. The injection process can be simulated with all the input parameters in Table.3.1, net pressure during fracture propagation can be generated for moderate plastic formation. In order to make the net pressure predicted by effective toughness method matches the net pressure in plastic formation; the effective toughness can be adjusted after each run until two curves finally close to each other. In this case, when the effective toughness was set to be 3 Mpa$\sqrt{m}$, which is 3 times higher than the original toughness, the net pressure simulated in elastic formation is almost the same as that in plastic formation with moderate yield strength, as shown in Fig.4.8. The net pressure curves also reveals that plasticity and increased toughness can lead to higher break down and propagation pressure.

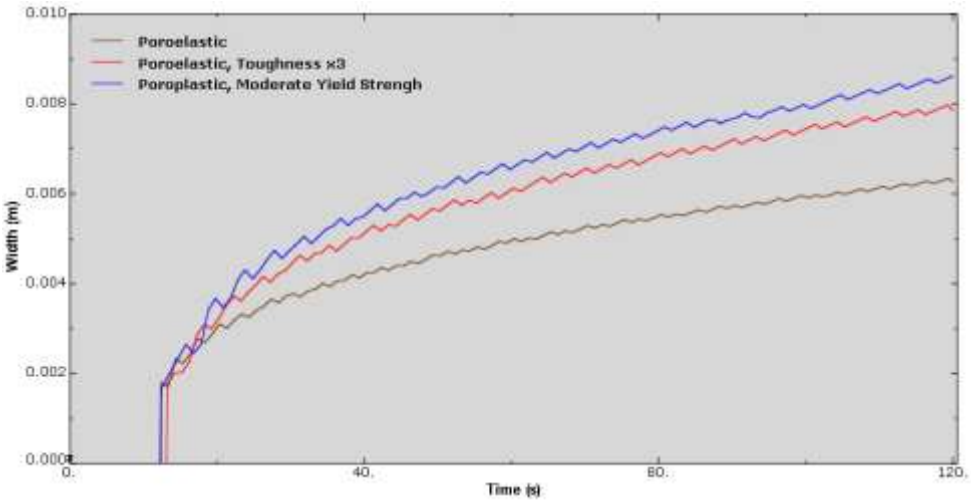

Figure 4.9 Maximum fracture width in elastic and plastic formations.

Both fracture geometry and net pressure are the most important output of hydraulic fracture model, net pressure and fracture geometry are closely related. Even though the method of effective toughness based on elastic model can generated the same net pressure as predicted by plastic model, however, the fracture is not the same in both model as shown in Fig.4.9. The fracture is wider in plastic formation than that in elastic formation with increased toughness. This discrepancy can be larger in formation with lower yield strength. Since the method of effective toughness only considers the plastic shielding effect at fracture tip, with lower yield strength, the plastic deformation zone will be larger around fracture. This account for shielding effect in front of fracture tip along, this will not be accurate enough to describe the whole plasticity effects. It can also be noted that both plasticity and increased toughness lead to wider fracture geometry.

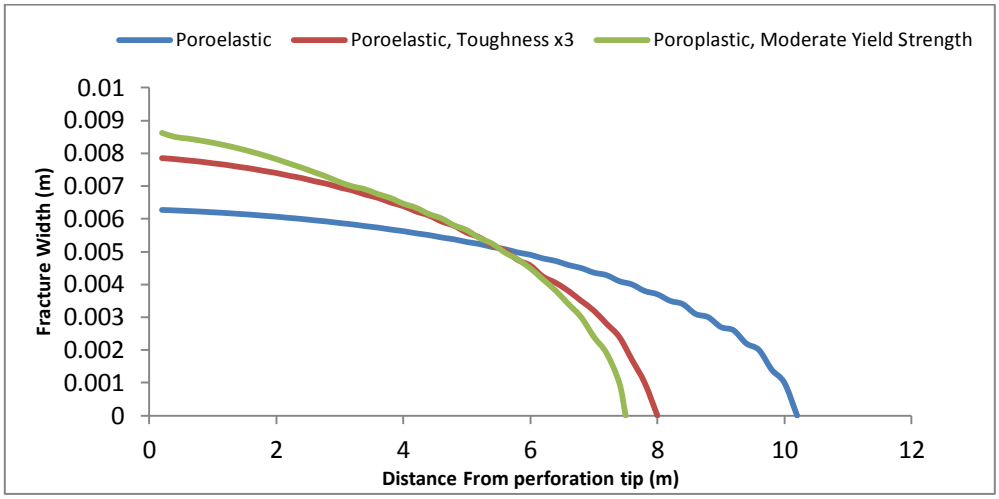

Figure 4.10 Fracture width profile along fracture path after 2 minutes injection.

The profile of fracture width predicted by different models was shown in Fig.4.10. It shows that the fracture is longest in poroelastic model with original toughness; the fracture length decreases if toughness was increased or plasticity was taken into consideration. The shorter the fracture length, and the wider the fracture will be created. When compare the results between poroplatic model and poroelastic model with increased toughness under the same net pressure, it should be noted that the fracture is wider in poroplastic model with the same net pressure, which is already demonstrated in Fig.4.8, and the fracture is also shorter in in poroplastic model. It suggests that the method of effective toughness can also result in shorter and wider fracture, but it can underestimate fracture width, and overestimate fracture length even if the predicted net pressure can match that in plastic formation, because it only account for the impact plastic deformation near the fracture tip. We can also notice that how big difference can be even in such a small treatment if we do not consider plasticity at all.

In all cases, the pressure drop along the fracture path is negligible, the pressure inside the fracture is all most equivalent to the pressure at wellbore except for area near fracture tip, this is because the fracture length is relative short and fluid viscosity is small,

and according the Equation (2.4), the biggest pressure drop happens at the fracture tip where the width vanishes to zero. The fluid pressure distribution in poroelastic formation is shown in Fig.4.11, the fluid pressure along the fracture remains almost the same and drops to formation pore pressure across the tip of fracture. The fluid pressure also drops to formation pore pressure in the direction that perpendicular to fracture surface, when the fluid leak-off into formation across filter cake. It can be also noted that the initial pore pressure is not affected by leak-off process in this circumstance.

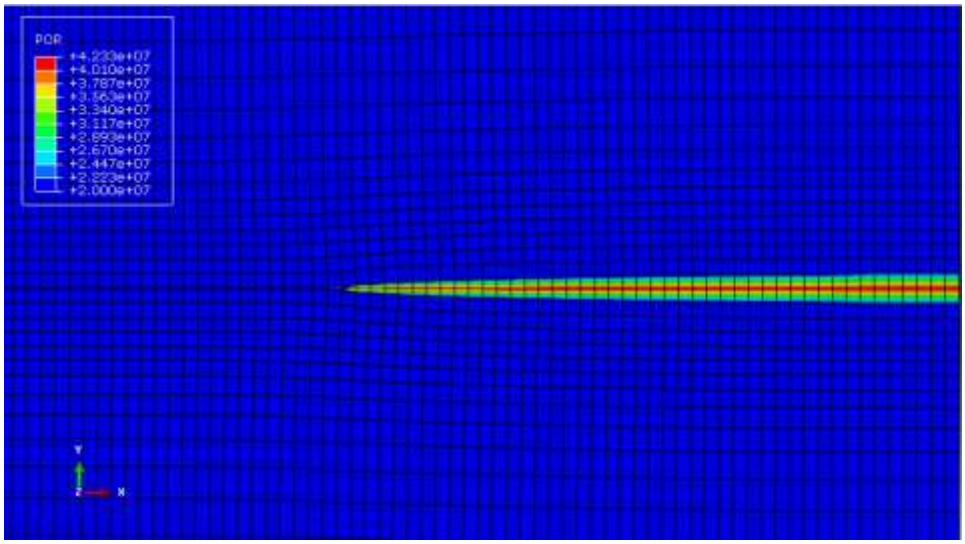

Figure 4.11 Fluid pressure distribution with 10md permeability.

Previous literature has demonstrated that wider fracture profiles are obtained with higher injection rates in poroelastic formation. In this study, we investigated how injection rate will affect fracture geometry and propagation pressure in plastic formation. Two different injection rates were simulated and the results are shown in Fig.4.12 and Fig.4.13. It demonstrates that that with higher injection rate, wider fracture profiles are obtained with faster propagation. Also larger zones of plastic deformation and higher net pressure are

observed. It can also be noted that with higher injection rate, less time is required to initiate the fracture propagation.

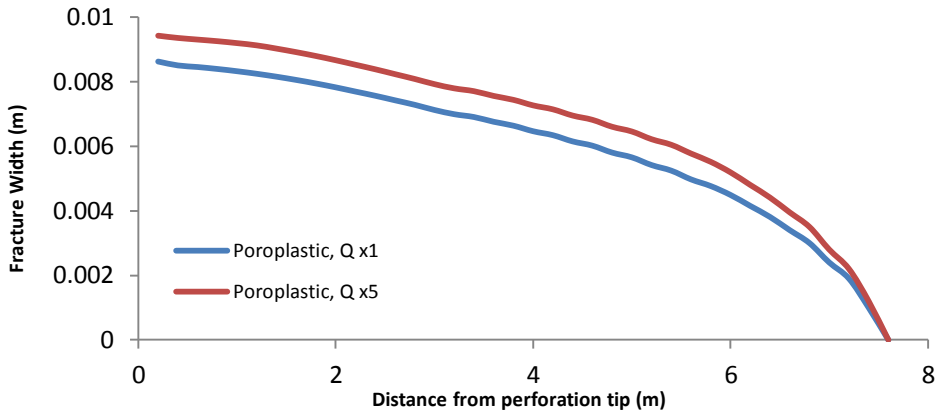

Figure 4.12 Maximum fracture width with different injection rate in plastic formation.

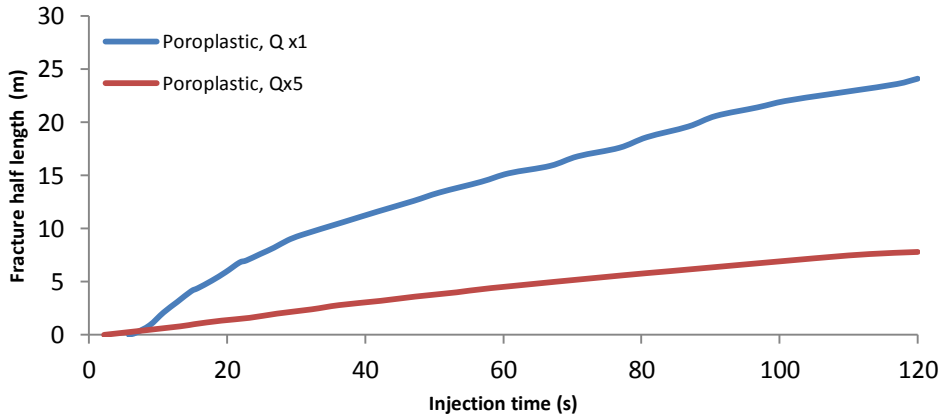

Figure 4.13 Fracture length with different injection rate in plastic formation.

Previous study has found that shear failure is observed to be the dominant failure mechanism in case of low efficiency fluids, with very little fracture growth in tensile mode. However, tensile fractures of considerable length surrounded by a zone of shear failure are obtained in the case of high efficiency fluids or in the case of fracture face plugging by particles present in the injected fluid. High leak-off leads to larger zones of material in a state of plastic shear due to pore pressure increase in the matrix.

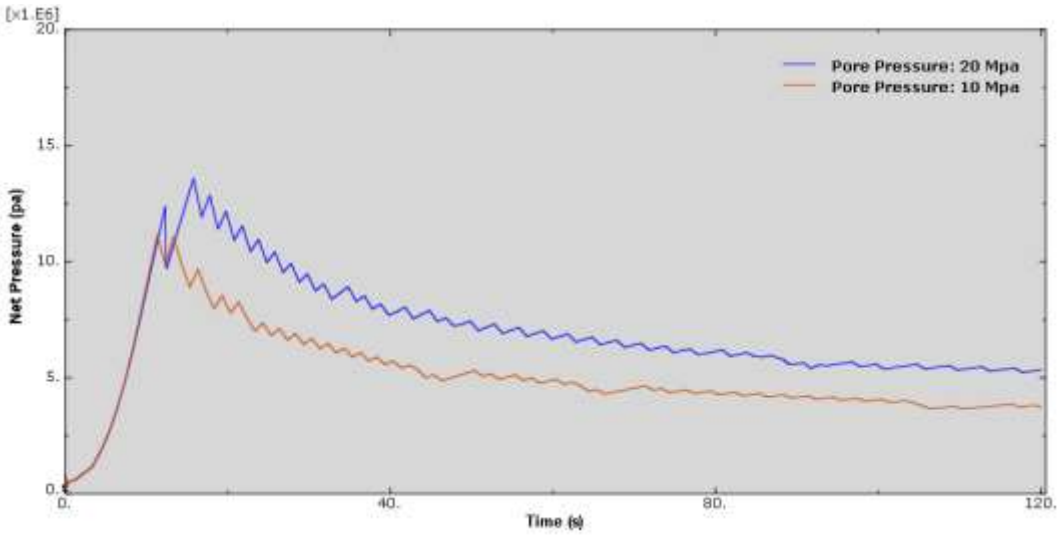

Figure 4.14 Fracture length with different injection rate in plastic formation.

In this study, we investigated how pore pressure in the formation can have impact on fracture geometry and net pressure in plastic formation. The pore pressure was set to be 10Mpa and 20 Mpa, respectively, and the far field in-situ stress remains the same. The simulation results were shown in Fig.4.14 and Fig.4.15. From Fig.4.14, we can see that higher pressure needed to propagate the fracture with increase pore pressure under the same far field stress, the implications that result in higher net pressure can be found in Fig.4.14, which shows that the higher the pore pressure, the larger the plastic deformation area around the fracture and hence, formation plasticity has greater impact on fracture geometry and net pressure, that leads to wider and shorter fracture. This result can also lead to the fact that for low efficiency fluid, high leak-off rate tend to increase pore pressure around fracture surface, result in larger plastic deformation zones and shear failure.

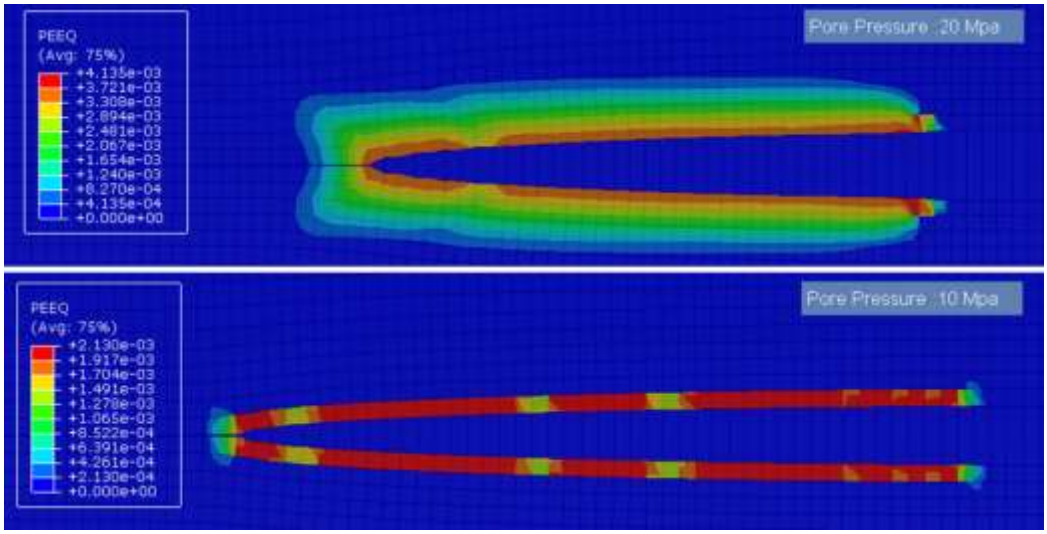

Figure 4.15 Plastic strain with different pore pressure.

There is no doubt that the closer the initial reservoir stress conditions to the shear failure surface, the more likely shear failure will be triggered around fracture during propagation. Next, we investigated how stress contrast can have impact on plastic deformation around fracture surface. Increase the horizontal stress contrast from 1.1 to 2 while all other parameters remain the same, the result shows in Fig. 4.16. Compared to Fig. 4.15, it be can be observed that higher contrast between the initial minimum and maximum total stresses can lead to wider plastic deformation area.

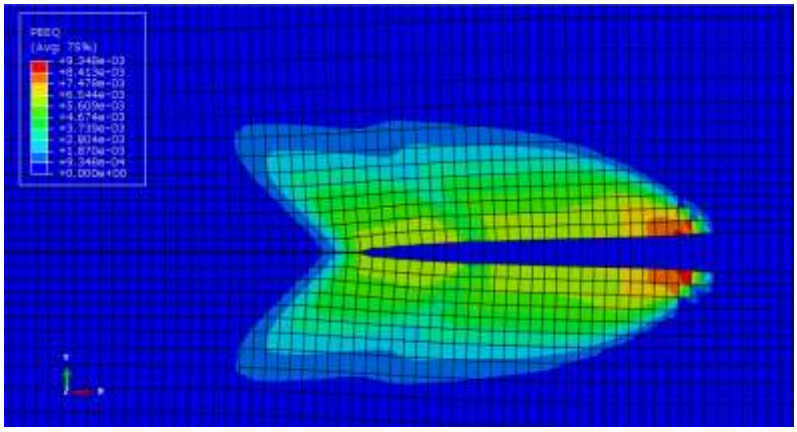

Figure 4.16 Plastic strain, horizontal stress contrast=2.

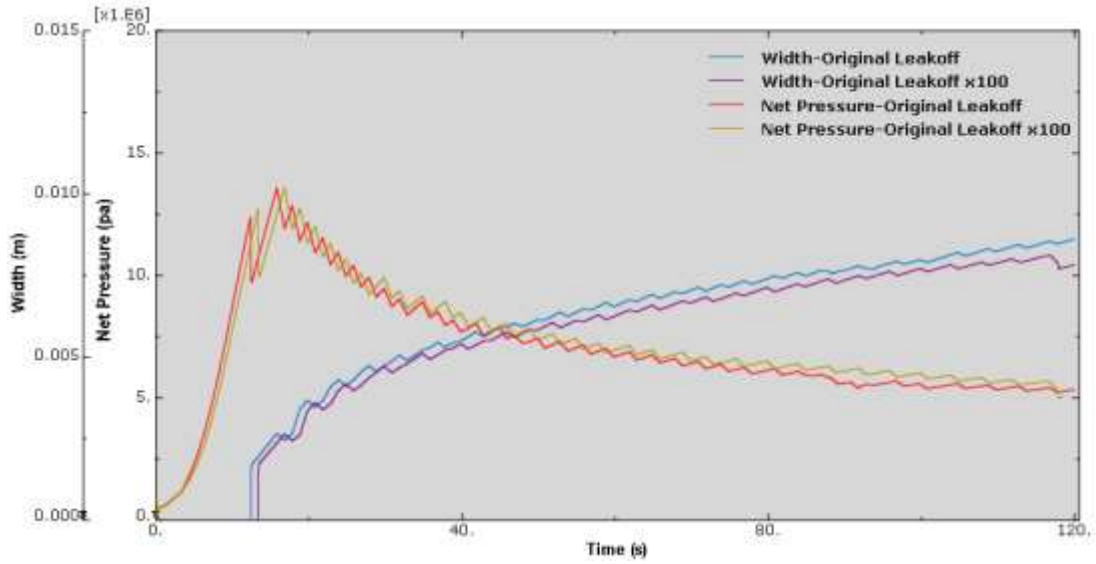

Figure 4.17 Net pressure and maximum width with different leak-off rate in plastic formation, k=10 md.

One important feature of poroelasticity is the fluid leak off into the formation porous media can develop backstress (changes in total stresses corresponding to changes in pore pressure) which reduces the differential pressures across the fracture face resulting in lower stress concentrations at the fracture tip. Here we investigate the how leak-off rate and formation permeability can contribute to poroelastic backstress, and in turn, affect fracture geometry and net pressure.

First, increase the leak-off coefficient 100 times, the results are compared with that of original leak-off coefficient. Higher leak-off rate can lead to much shorter fracture length with the same injection rate, but only have limited impact on net pressure and fracture width, as shown in Fig.4.17. Slightly higher net pressure and smaller fracture width are obtained with higher leak-off rate because of poroelastic backstress. Even though the leak-off rate increase 100 times, but the permeability is still large enough to allow the pore fluid to move

freely and dissipate energy at the same time scale as the fracture opening, so the pore pressure around the fracture can be considered nearly constant and poroelastic backstress induced by leak off volume and plastic deformation affected by changes of pore pressure is relative small.

Next, remain the original leak-off rate but change the formation permeability from 10md to 0.001md. The simulation results were shown in Fig.4.18. It can be observed that a large net pressure increase is observed in lower permeability formation, but only small changes occur in fracture width. This is because that pore pressure increased significantly around the fracture surface because of low permeability impeded the diffusion process even with original low leak-off rate, as shown in Fig.4.19. We can see that the pore pressure around the fracture is almost 5 Mpa higher than original pore pressure. The increased pore pressure around fracture leads to larger zones of plastic deformation and poroelastic backstress, which in turn, contributes to higher net pressure. However, the difference between fracture widths is small due the large poroelastic backstress, which offset some effect of higher net pressure and larger plastic deformation.

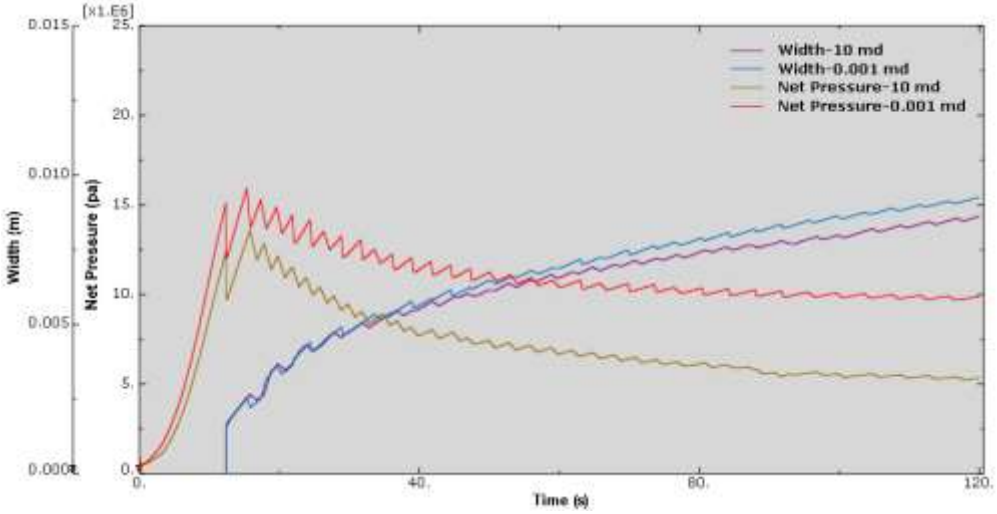

Figure 4.18 Net pressure and maximum width with different permeability in plastic formation, C_L= 2E-6 m/$\sqrt{s}$.

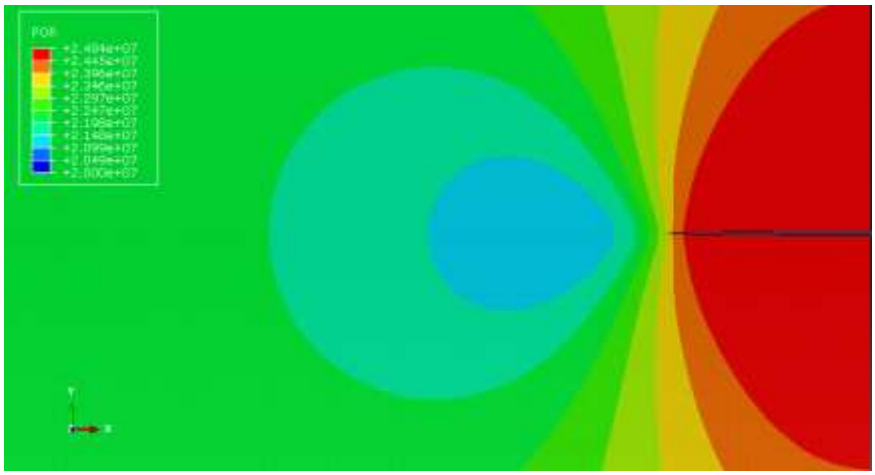

Figure 4.19 Fluid pressure distribution in formation matrix, k=0.001.

In this study, we also found non-wetting zone can be developed at the fracture tip in low permeability formation when fracture propagates quicker than the fracture fluid can fill up new fracture volumes that are created at the tip of a propagating fracture. This is manifested by negative pressures develop at the tip of a propagating fracture as shown in Fig.4.20, the formation permeability was reduced to 0.0001 md and injection rate was increased to 0.05 m^3/s/unit height.

A dry zone may occur at the fracture tip in a physical application because the fracture is running ahead of the viscous fluid, or a dry zone may also arise because of the numerical technique that is used for fracture propagation. A dry zone will develop as an artifact of the numerical technique when nodes are released at the beginning of a time step and the time step size is too small for the fluid to fill up the newly created fracture cells. For a dry zone to develop, the program allows cells in the fracture to be partially saturated with fluid. The fluid pressure in a partially saturated cell is prescribed to have a constant value until the cell fills completely with fluid.

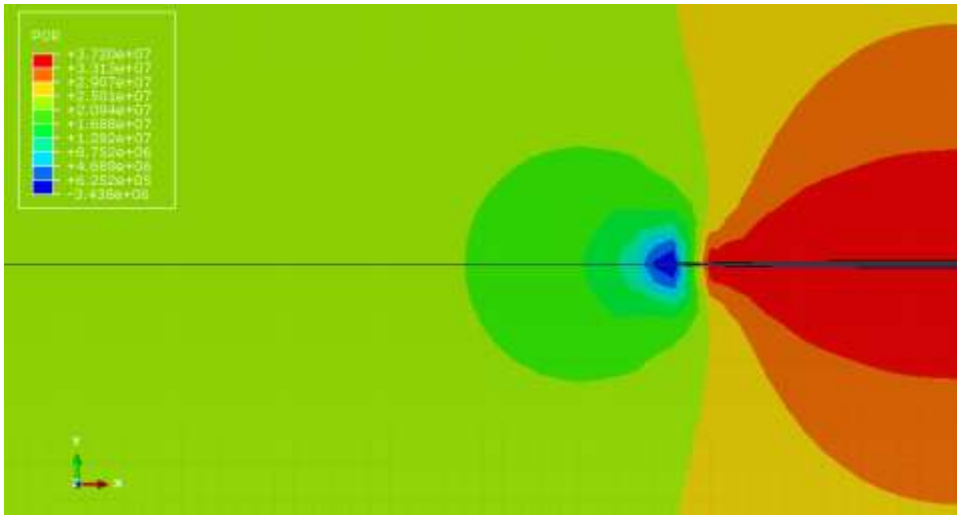

Figure 4.20 Non-wetting zone in front of fracture tip.

Three types of plastic formations with different yield strength were investigated to reveal how plastic property itself can have impact fracture geometry and net pressure. The cohesion yield strength of 3 types of formations are 2 MPa, 4 MPa and 6 MPa respectively, which represent formations with relative low, moderate and high yield strength in this study. The simulation results of plastic strain and affected area were shown from Fig.4.21 to Fig.4.22.

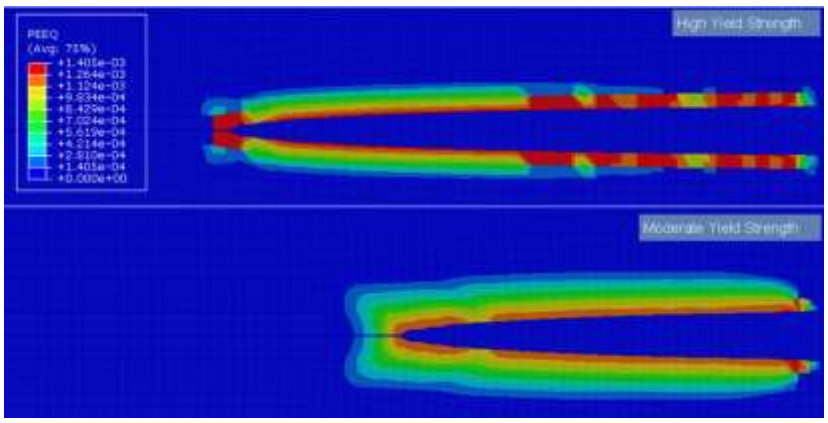

Figure 4.21 Plastic strain with high and moderate yield strength.

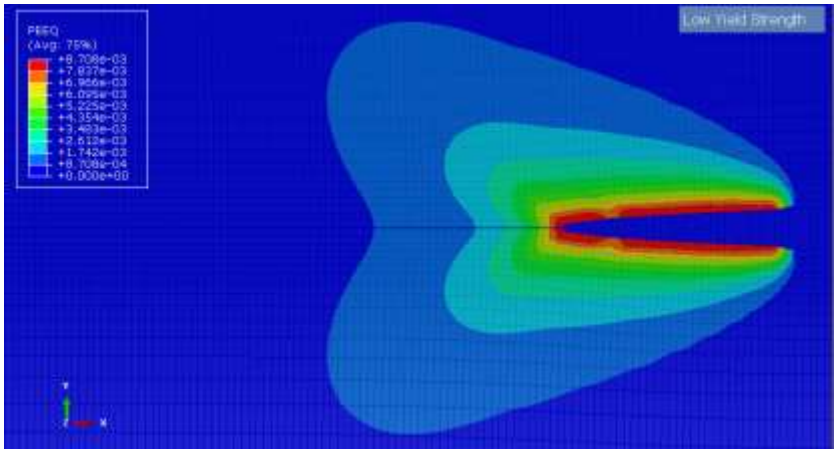

Figure 4.22 Plastic strain with low yield strength.

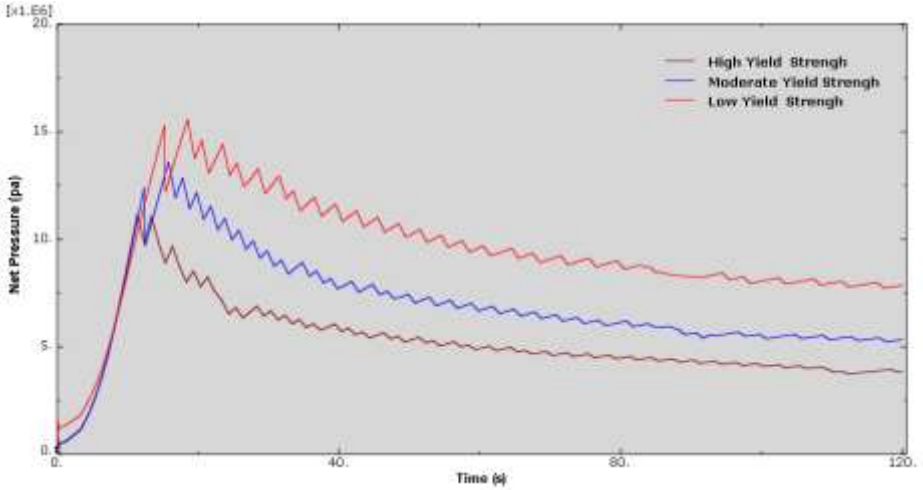

Figure 4.23 Net pressure with different yield strength.

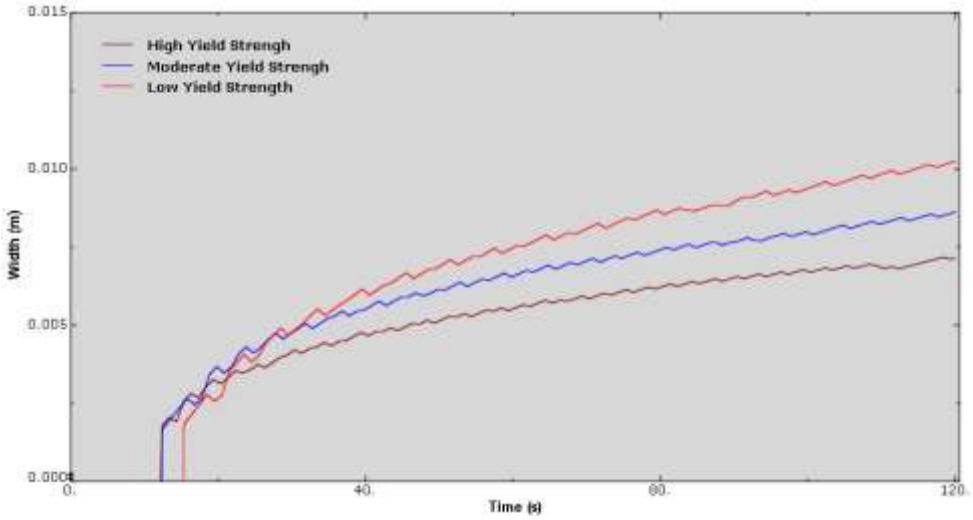

Figure 4.24 Fracture width at wellbore with different yield strength.

It shows that the more plastic the formation (with decreasing yield strength), the larger the area affected by plastic deformation, and the shorter the fracture length. The area that undergo through plastic deformation are within 0.4m and 1 m around fracture path in formation with high and moderate yield strength, but it can extend to a few meters in formation with relative low yield strength. It was also found the more plastic the formation, the higher the propagation pressure are needed and wider fracture are created, as shown in Fig.4.23 and Fig.4.24.

4.3 Long Term Injection

In the second case, a 30-minute injection was simulated, with Carter's leak-off coefficient $2 \times 10^{-4}\ \mathrm{m}/\sqrt{s}$ and 10md permeability, in which case the effect the poroelastic backstress is negligible. The fracture length and fracture width are inherent solutions of each time increment in all models. The total injection fluid can be calculated from injection rate and pump schedule, the total leak-off volume can be calculated based on equation (2.5) by integrating the entire fracture surface domain.

To investigate the impact of deviations of fracture geometry on production, the Unified Fracture Design (UFD) approach (Economides et al., 2002a) was used, The central idea of the UFD technique is to select the appropriate optimum compromise between propped fracture length and width, for a given proppant volume and depending on the properties of the reservoir and the selected proppant. To determine the volume of proppant reaching the target layer in a two-dimensional calculation, the fracture height must be a known quantity, predicted or presumed. Then

$$V_p = \frac{M_p(\frac{h}{h_f})}{\rho_{prop}(1-\emptyset_{prop})}\,. \tag{4.1}$$

The next step is to calculate the Proppant Number:

$$N_p = \frac{4k_f x_f w}{k x_e^2} = \frac{4k_f x_f w h_p}{k x_e^2 h_p} = \frac{2k_f V_p}{k V_{res}}\,, \tag{4.2}$$

where V_p is the propped volume inside the pay as calculated from Eq. (4.1) and V_{res} is the drainage volume of the reservoir. From the value of N_p the maximum J_D can be determined, as can the optimum fracture conductivity, $C_{fd,opt}$ (Economides et al, 2002a). For a square drainage area, the maximum achievable dimensionless pseudosteady-state productivity index as a function of the Proppant Number is given by

$$J_{D,max}(N_p) = \begin{cases} \dfrac{1}{0.990 - 0.5\,\mathrm{In}(N_p)} & \text{if } N_p \le 0.1 \\ \dfrac{6}{\pi} - \exp\left[\dfrac{0.423 - 0.311N_p - 0.089{N_p}^2}{1 + 0.667N_p + 0.015{N_p}^2}\right] & \text{if } N_p \le 0.1 \\ \dfrac{6}{\pi} & \text{if } N_p \ge \sim 100 \end{cases}. \tag{4.3}$$

Similarly, the optimal dimensionless fracture conductivity for the entire range of Proppant Numbers is given as

$$C_{fD,opt}(N_p) = \begin{cases} 1.6 & \text{if } N_p < 0.1 \\ 1.6 + \exp\left[\dfrac{-0.583 + 1.48\,\mathrm{In}(N_p)}{1 + 0.142\mathrm{In}(N_p)}\right] & \text{if } 0.1 \le N_p \le 10\,. \\ N_p & \text{if } N_p > 10 \end{cases} \tag{4.4}$$

Once the optimal dimensionless fracture conductivity is known, the optimal fracture length and width can be readily determined:

$$x_{f,opt} = \sqrt{\frac{k_f V_f}{2C_{fD,opt}kh}} \qquad and \tag{4.5}$$

$$w_{opt} = \sqrt{\frac{C_{fD,opt} k V_f}{2 k_f h}} \ . \tag{4.6}$$

Fig.4.25 shows the relationship J_D and C_{fD} for a range of Proppant Numbers.

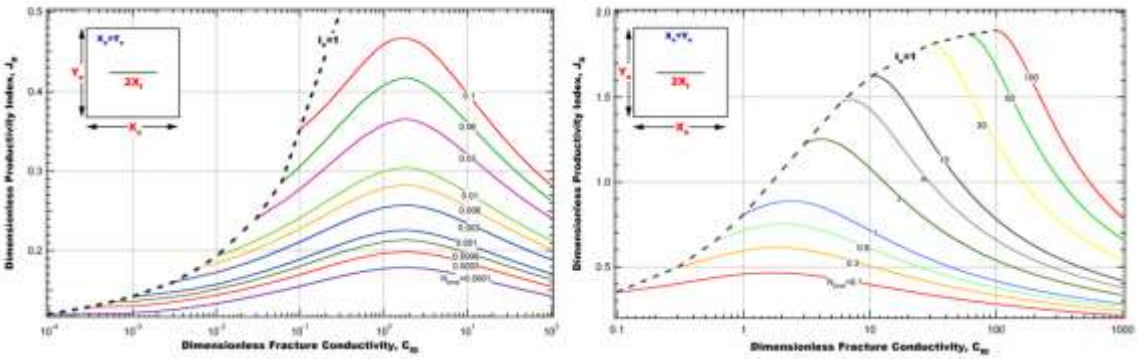

Figure 4.25 Relationship between dimensionless productivity index and dimensionless fracture conductivity.

The real fracture geometry that deviated from the optimal design because of formation plasticity can lead to suboptimal dimensionless fracture conductivity, C_{fD}, which can result in reduction of dimensionless production index, J_D. The dimensionless fracture conductivity can be calculated by

$$C_{fD} = \frac{k_f w}{k x_f} \ . \tag{28}$$

Table 4-1 represents the input data for Unified Fracture Design presented in this work. Based on the input data the optimum fracture geometry that provides the maximum dimensionless productivity index can be determined. The fracture propagation model is run independently until its output matches the conclusions of the UFD.

Table 4-1 Reservoir and fracture input data for the fracture designs

Drainage area, acre	320
Net thickness, *h*, ft	100
Fracture height, h_f, ft	100

Well radius, r_w, ft	0.3
Proppant mass, M_p, lbm	200,000
Porosity of proppant pack	0.36
Specific gravity of proppant	2.65
Proppant pack permeability, k_f, md	115,000
Reservoir Permeability, k, md	10

The simulation results are shown in Table 4-2. From these results, we can see that the plasticity can have a substantial impact on fracture geometry after 30 minutes of injection. The fracture length can be reduced by nearly 38 % compared to the predicted value in elastic formation in this study. In addition, the fluid efficiency increases in the plastic formation because the shorter fracture length results in a smaller leak-off surface. These results also indicate that the effective toughness method can underestimate fracture width and overestimate fracture length even if it can accurately match the net pressure in the plastic formation, because it only accounts for shielding effects of the process zone in front of the fracture tip and fails to take the entire plastic zone into consideration.

Table 4-2 Simulation results of 30-minute injection

	Optimum Design	Poroelastic	Poroelastic, K_{IC}x3	Poroplastic, Moderate Yield Strength
N_p	0.03			
Fracture Length (m)	79.8	80.6	58.8	50.2
Fracture Width (mm)	11.43	11.52	16.95	20.67
Fluid Efficiency %	73.87	75.20%	80.72%	84.06%
C_{fD}	1.6	1.6	3.3	4.7
J_D	0.37	0.37	0.34	0.33
J_D Reduction %	0	0	8.1	10.8

From a production point of view, a 30-minute injection schedule can generate nearly optimal fracture geometry in elastic formation with maximum dimensionless productivity

index. However, if the formation exhibits plastic behavior, the real fracture geometry will be suboptimal and the dimensionless productivity index, J_D, is 10% lower than the optimal value. The reduction in J_D can be more severe in unconventional reservoirs where formation permeability is extremely low. From Eq.(23), the lower the formation permeability the higher the Proppant Number. The Proppant Number increases to 3.2 by reducing the formation permeability to 0.1 md in Table.2. If the dimensionless fracture conductivity, C_{fD} , is 3 times higher than the optimum value (the same ratio in Table 3) then from Fig.25, it can be seen that the deviation from optimal fracture geometry can lead to nearly 20% reduction in J_D. In the case of lower cohesion strength formation rock, subjected to higher in-situ stress and horizontal stress contrast, the fracture half-length can be reduced to around 40% of that predicted by the elastic model, which can lead to the dimensionless fracture conductivity, C_{fD} , that is 6~7 times higher than the optimal value leading to a 40~50% reduction in the J_D. Thus reduction in fracture length because of plasticity has much greater impact on the well production in a low permeability reservoir than that in a high permeability reservoir.

5. CONCLUSIONS AND REMARKS

5.1 Conclusions

In this study, we developed a numerical model of hydraulic fracture based on cohesive zone finite element method to investigate fracture propagation in elastic and plastic formations. Solid deformation, fluid flow inside fracture and fluid diffusion process are fully coupled in this model. The impact of formation plastic properties on fracture process is investigated for both short term and long term injection and the results are compared with elastic formation. In addition, the main factors that affect the impacts of poroelastic backstress and formation plasticity on hydraulic fracture are also investigated. From the results of this research, we can conclude that:

1. In a plastic formation, net-pressure drops to zero while the fracture is still open along a proportion of the original length; the fracture will close completely at negative net pressure when fluid pressure inside the fracture is less than far-field minimum horizontal stress.
2. In comparison to hard rock, plastic and highly deforming formations have exhibited higher breakdown and injection pressures. The more plastic the formation (lower cohesion strength), the higher is the net pressure required to propagate the fracture due to increased plastic deformation, which leads to shorter and wider fracture. Under the same net pressure, a fracture in a plastic formation is wider than that in an elastic formation. This discrepancy is larger in a formation with lower yield strength where a larger area undergoes plastic deformation.

3. The effects of formation plasticity on a hydraulic fracture are mostly controlled by in-situ stress, the plastic property and pore pressure. The closer the initial stress value is to the shear failure value and the greater the total stress contrast, the more likely shear failure will be triggered around fracture. With the same far-field stress and formation properties, pore pressure can play an important role on the fracture process in a plastic formation. When pore pressure increases, net pressure increases due to larger zones of plastic deformation because of strong fluid/solid coupling.
4. Poroelastic backstress is mostly controlled by leak-off rate and formation permeability. When the leak-off rate is relatively high and the formation permeability is not large enough to allow pore fluid to move freely and dissipate energy at the same rate as the fracture opening, the pore pressure around the fracture will increase and induce compressive stress on the fracture surface.
5. Both poroelastic backstress and formation plasticity can contribute to a higher net pressure, but they have a different impact on fracture width. Poroelastic backstress tends to reduce fracture width, while plasticity tends to increase fracture width.
6. Non-wetting zone can be developed ahead of the fracture tip in low permeability formations when a fracture propagates quicker than the fracture fluid can fill up newly created micro-cracks.
7. Ignoring plasticity in plastic formation can lead to inaccuracy of fracture geometry, net pressure prediction and fluid efficiency calculation. The deviations of real fracture geometry from elastic formation model can have great impact on well production, especially in unconventional, low permeability reservoirs.

REFERENCES

Nemat-Nasser, Hirakawa. 1983. Hydraulic Fracturing and Geothermal Energy. Martinus Nijhoff, The Hague.

Murdoch. L.C. 1992. Hydraulic Fracturing of Soil during Laboratory Experiments Part 1. Methods and Observations. Geotechnique Vol. 43, No. 2.pp. 255-265.

Adachi,J., Siebrits, E., Peirce, A., and Desroches, J., 2007. Computer Simulation of Hydraulic Fractures. International Journal of Rock Mechanics & Mining Sciences 44(5): 739-757.

Khristianovic, S. and Zheltov, Y. 1955. Formation of Vertical Fractures By Means of Highly Viscous Fuids. In Proc. 4th World Petroleum Congress, Rome, volume II, pages 579–586.

Geertsma, J. and de Klerk, F. 1969. A Rapid Method of Predicting Width and Extent of Hydraulic Fracture. J. Pet. Tech., Trans. AIME, 222:937–949.

Nordgren, R. 1972. Propagation of Vertical Hydraulic Fractures. J. Pet. Tech., 253:306–314.

Sone, H., Zoback, M.D 2011 .Visco-plastic Properties of Shale Gas Reservoir Rocks. 45th U.S. Rock Mechanics / Geomechanics Symposium, June 26-29, 2011, San Francisco, California

Papanastasiou, P., and Thiercelin, M. 1993. Influence of Inelastic Rock Behavior in Hydraulic Fracturing.. Int. J. Rock Mech. Min. Sci. Geomech. Abstr., 30(7), 1241 – 1247

Papanastasiou, P. 1997. The Influence of Plasticity in Hydraulic Fracturing. Int. J. Fract., 84(1), 61 – 79

Papanastasiou 1998.The Effective Fracture Toughness in Hydraulic Fracturing. Int. J. Fract., 96(1), 127 – 147

Germanovich, L. N., Astakhov, D. K., Shlyapobersky, J., Mayerhofer, M. J., Dupont, C., and Ring, L. M. 1998. Modeling Multi-segmented Hydraulic Fracture in Two Extreme Cases: No Leak-off and Dominating Leak-off. Int. J. Rock Mech. Min. Sci., 35(4 – 5), 551 – 554

Papanastasiou, P. 1999a. The Effective Fracture Toughness in Hydraulic Fracturing. Int. J. Fract., 96(2), 127 –147

Haimson, B., and Fairhurst, C. 1967. Initiation and Extension of Hydraulic Fractures in Rocks. Society of Petroleum Engineers Journal, Volume 7, issue 3.

Muskhelishvili, N.I., Radok, J.M.R, 1953. Some Basic Problems of The Mathematical Theory of Elasticity. Cambridge Univ Press

Horsrud, P., Risnes, R., and Bratli, R.K. 1982. Fracture Initiation Pressures in Permeable Poorly Consolidated Sands, International Journal of Rock Mechanics and Mining Sciences & Geomechanics Abstracts, 255-266

Wang, Y,. Dusseault, M.B. 1991. International Journal of Rock Mechanics and Mining Sciences & Geomechanics Abstracts, 235-246, Volume 28, issue 4.

Murdoch, L. C., 1993a. Hydraulic Fracturing of Soil during Laboratory Experiments, Part I Methods and observations, Geotechnique, 43, 255-265

Murdoch,L. C., 1993b. Hydraulic Fracturing of Soil during Laboratory Experiments, Part II Propagations, Geotechnique, 43, 267-276

Murdoch,L. C., 1993c. Hydraulic Fracturing of Soil during Laboratory Experiments, Part III Theoretical Analysis, Geotechnique, 43, 277-287

Mori, A. and Tamura, M., 1987. Hydrofracturing Pressure of Cohesive Soils, Solis and Foundations 27, 14-22

Jaworski, G. W., Duncan, J. M., and Seed, H. B., 1979. An Experimental Study of Hydraulic Fracturing, Report UCB/GT/79-02, P. 234, Denver

Dam, D. B., Papanastasiou, P., and Pater, C. J., 2000. Impact of Rock Plasticity on Hydraulic Fracture Propagation and Closure. SPE Annual Technical Conference and Exhibition, Dallas Texas, October 2000

Dam, D.B., and de Pater, C.J., 2001. Roughness of Hydraulic Fractures: Importance of In-Situ Stress and Tip Processes, SPE Journal, 6(1)

Hillerborg, A., Modeer, M., and Petersson, P.E., 1976.Analysis of Crack Formation and Crack Growth in Concrete by Means of Fracture Mechanics and Finite Elements. Journal of cement and concrete research, 773-781

Zhai, Z. and Sharma, M. M., 2005.A New Approach to Modeling Hydraulic Fractures in Unconsolidated Sands. Paper SPE 96246 presented at the SPE Annual Technical Conference and Exhibition, Dallas, Texas, 9-12 October

Wu, R., 2006. Some Fundamental Mechanisms of Hydraulic Fracturing, Ph.D. thesis, 280 pp., Georgia Institute of Technology, USA

Dean RH, Schmidt JH. 2009. Hydraulic Fracture Predictions With A Fully Coupled Geomechanical Reservoir Simulator. Soc Petroleum Eng J 14(4):707–714

Vyacheslav Mokryakov.2011. Analytical Solution for Propagation of Hydraulic Fracture with Barenblatt's Cohesive Tip Zone" Int J Fract (2011) 169:159–168

E. Sarris,P. Papanastasiou .2012. Modeling of Hydraulic Fracturing in a Poroelastic Cohesive Formation. International Journal of Geomechanics , Vol. 12, No. 2, April 1, 2012

YaoYao. 2012. Linear Elastic and Cohesive Fracture Analysis to Model Hydraulic Fracture in Brittle and Ductile Rocks" Rock Mech Rock Eng (2012) 45:375–387

Brodkev. R.S. 1967. The Phenomena of Fluid Motion. Addison-VVeslev. Reading. MA

Barree, R.D. 2007. Fracturing Materials. keynote address, SPE Hydraulic Fracturing Conference, The Woodlands, TX, January 19-21

Whittaker. A., (ed.) 1985. Theory and Application of Drilling Fluid Hydraulics. IHRDC Publishers. Boston, MA

Daneshy, A.A. 1989. Proppant transport. In Recent Advances in Hydraulic Fracturing, SPE monograph. Vol. 12. pp. 210-222

Boone TJ, Wawrzynek PA, Ingraffea AR. 1986. Simulation of Fracture Process in Rock with Application to Hydrofracturing. Int J Rock Mech Min Sci Geomech Abstr 23:255–265

Boone JT, Ingraffea AR. 1990. A Numerical Procedure for Simulation of Hydraulically Driven Fracture Propagation in Poroelastic Media. Int J Numer Anal Methods Geomech 14:27–47

Howard. G.C. & Fast. C.R. 1970. Hydraulic Fracturing. SPE monograph. Vol. 2. Henry L. Doherty series.

Cheng, A.H.-D.. Abousleiman, Y. Roegiers, J.-C. 1993. Review of Some Poroe-lastic Effects in Rock Mechanics. Proc. 34th U.S. Rock Mech. Svmp., Madison, Wisconsin, pp. 1119-1126

Jaeger, J. C., Cook, N. G. W. and Zimmerman, R.W. 2007. Fundamentals of Rock Mechanics, Fourth Edition. Blackwell Publishing, 475 pp

Barenblatt GI .1959. The Formation of Equilibrium Cracks During Brittle Fracture: General Edeas and Hypothesis, Axially Symmetric Cracks. Appl Math Mech (PMM) 23:622–636

Barenblatt GI .1962. The Mathematical Theory of Equilibrium Cracks in Brittle Fracture. Adv Appl Mech 7:55–129

Dugdale DS .1960. Yielding of Steel Sheets Containing Slits. J Mech Phys Solids 8:100–104

Boone TJ, Wawrzynek PA, Ingraffea AR .1986. Simulation of Fracture Process in Rock with Application to Hydrofracturing. Int J Rock Mech Min Sci Geomech Abstr 23:255–265

Boone JT, Ingraffea AR .1990. A Numerical Procedure for Simulation of Hydraulically Driven Fracture Propagation in Poroelastic Media. Int J Numer Anal Methods Geomech 14:27–47

Zienkiewicz OC and Taylor RL .2005. The Finite Element Method (5th edition), Vol1, the basis, Elsevier Pte Ltd, London, pp 42-45

Griffith AA .1921. The Phenomena of Rupture and Flow in Solids. Phil Trans R Soc 221:163–198

Griffith AA .1924.The Theory of Rupture. In: Proceedings of 1st International Congress for Applied Mechanics, Delft, The Netherlands, pp 55–63

Camanho, P. P., and C. G. Davila, 2002. Mixed-Mode Decohesion Finite Elements for the Simulation of Delamination in Composite Materials. NASA/TM-2002–211737, pp. 1–37, 2002

Kanninen, M. F., and Popelar, C. H. 1985. Advanced Fracture Mechanics. Oxford Univ., UK

Lim IL, Johnston IW, Choi SK, Boland JN .1994. Fracture Testing of a Soft Rock with Semi Circular Specimens under Three-point Bending Part 2—Mixed Mode. Int J Rock Mech Min Sci 31(3):199–212

Benzeggagh, M. L., and M. Kenane. 1996. Measurement of Mixed-Mode Delamination Fracture Toughness of Unidirectional Glass/Epoxy Composites with Mixed-Mode Bending Apparatus. Composites Science and Technology, vol. 56, pp. 439–449, 1996

Turon, A., Camanho, P.P., Costa, J., Davila, C.G. 2006. A Damage Model for The Simulation of Delamination in Advanced Composites under Variable-Model Loading. Mech. Mater. 38 (11), 1072–1089